DEM Generation from Multi-View Satellite Images in Sub-Sahel Region

*Original*
DEM Generation from Multi-View Satellite Images in Sub-Sahel Region / Abraiz, Muhammad; Belcore, Elena; Piras, Marco. - In: INTERNATIONAL ARCHIVES OF THE PHOTOGRAMMETRY, REMOTE SENSING AND SPATIAL INFORMATION SCIENCES. - ISSN 2194-9034. - ELETTRONICO. - XLVIII-M-6-2025:(2025), pp. 9-14. ( Topographic Mapping from Space” dedicated to Dr. Karsten Jacobsen’s 80th Birthday Istanbul Turchia 29-31 January 2025) [10.5194/isprs-archives-xlviii-m-6-2025-9-2025].

*Availability:*
This version is available at: 11583/3000319 since: 2025-05-20T16:10:17Z

*Publisher:*
Umut Güne Sefercik

*Published*
DOI:10.5194/isprs-archives-xlviii-m-6-2025-9-2025

Progress in Additive Manufacturing
https://doi.org/10.1007/s40964-025-01388-8

RESEARCH

# Effect of 3D grading thickness on mechanical and deformation behaviour of gyroid structures produced via powder bed fusion with electron beam

**Danilo Bruson**[1] · **Giovanni Rizza**[1] · **Manuela Galati**[1]

Received: 30 April 2025 / Accepted: 6 October 2025

## Abstract

The production of complex geometries with geometrical tuned features is made possible by Additive manufacturing (AM) processes. Powder Bed Fusion using Electron Beam (PBF-EB) is one of the AM techniques for metallic components, which stands out for its ability to fabricate intricate structures with high-performance materials. One example is surface-based architectures known as Triply Periodic Minimal Surfaces (TPMS), where structural walls are defined by a specific thickness. The mechanical behaviour and deformation mechanisms of TPMS are governed by both the geometry and the wall thickness of the structure. Conventional TPMS designs typically employ a uniform or one-dimensional thickness gradient, which constrains their performance under varied loading conditions. This study explores a novel approach involving three-dimensional thickness gradation, aiming to enhance structural integrity, improve load-bearing capacity, and enable functional optimisation. The gyroid surface, a widely studied TPMS for applications ranging from lightweight aerospace components to biomedical implants, is used as a reference geometry. Three types of initiator surface (diagonal plane, cross-shape, and sphere) are employed to create spatial variations in wall thickness between predefined minimum and maximum values. Samples are fabricated using the PBF-EB process, and the resulting structures are characterised via X-ray computed tomography to assess morphometric parameters. These parameters are then correlated with mechanical properties and deformation mechanisms and compared against gyroid TPMS with uniform thickness. The results reveal a significant influence of 3D thickness variation on performance, offering new insights for the design and additive manufacturing of next-generation TPMS structures with tailored mechanical responses.

**Keywords** EBM · Digital image correlation · Tomography · Gyroid · 3D density grading

## 1 Introduction

The answer of nature when a stiff but light structure is required is a cellular structure. Cellular structures were initially identified by Robert Hooke [1] when observing natural elements using a magnifying glass. In his observations, Hooke discovered that the microstructure of elements as wood, bones or leaves is composed of porous hierarchical architectures in contrast to the common belief of fully dense matter. The first engineering structures inspired by Hooke's discoveries were the stochastic metal foams [2] with structural, functional, biomedical and chemical applications. These structures were characterised by a deformation behaviour that is different from that of the bulk (fully dense) material and that can be controlled by the structure geometry. A great contribution to the investigation of the deformation and mechanical properties of these structures was given by Gibson, Ashby and team [3–5]. The desire for control of the mechanical properties and deformation behaviour pushed the research toward non-stochastic structures, generally identified as lattice structures. Lattice structures are topologically ordered structures obtained with the repetition of a unit cell in space [6]. The attention of the research

---

✉ Danilo Bruson
danilo.bruson@polito.it

Giovanni Rizza
giovanni.rizza@polito.it

Manuela Galati
manuela.galati@polito.it

[1] Department of Management and Production Engineering (DIGEP), Integrated Additive Manufacturing Center (IAM@PoliTo), Polytechnic University of Turin, Corso Duca degli Abruzzi 24, 10129 Turin, Italy

toward these structures is constantly growing due to the high strength to weight ratio, the capability to absorb a large amount of energy, a good thermal exchange capability and acoustic and vibration dumping. A summary of examples of applications of these structures can be found in detailed literature reviews [6–8].

Depending on the unit cell, lattice structures are generally classified as strut-based or surface-based structures [9]. The unit cell of the strut-based structures is composed of a series of trusses connected at nodes with varying thickness, length and orientation [10]. The unit cell of surface-based structures is composed of a set of points equidistant from a guiding surface described by a periodic equation. The distance of the points from the guiding surface is defined as the wall thickness of the structure. The guiding surface is usually a triply periodic minimal surface (TPMS), because it has a zero mean curvature at each point, it is not self-intersecting and repeats periodically in three independent spatial directions [11]. The characteristic of a near zero mean curvature is of particular interest for biomedical applications, since it mimics the bone structure [12, 13] and facilitates the bone adhesion and growth [14]. In addition, TPMS structures are more appealing than strut-based structures because they have a large energy absorption capacity [15], there are no sharp angles and possess superior fatigue resistance [16].

Because of such 3D geometrical complexity, the manufacturing of these structures is difficult and therefore today is limited to additive manufacturing (AM) techniques [17]. Among those techniques, powder bed fusion with electron beam (PBF-EB) is particularly suited to the production of metallic complex structures for several reasons. The vacuum in the chamber preserves material from oxidation and gas contamination while the permanence in the hot environment acts as a stress relief treatment, preventing distortions of the structures [18]. The high temperature during the process, obtained with a preheating step prior to melting, also produces a partial sintering of the powder particles, which results in being strong enough to support the construction [19]. Sintered powder has a larger thermal conductivity [20] than the loose powder, which helps to prevent thermal imbalance and deformations or stress accumulation in the molten cross section. Several studies in the literature investigated the production of TPMS structures using the PBF-EB process [17, 18, 21–28]. Most of the studies available in the literature investigated structures with a constant thickness [18, 22–24, 27] ranging from 0.31 mm [24] to 1.01 mm [22]. The minimum wall thickness is related to the machine constraints and the process parameters adopted from production. In the case of structures with a designed wall thickness approaching the minimum electron beam diameter (approximately 400 µm [29]), the effective wall thickness tends to the beam diameter, resulting in a smaller or larger wall thickness than the designed wall thickness. As an example, Khrapov et al. [23] and Polley et al. [27] designed structures with a nominal wall thickness varying from 0.1 mm to 0.4 mm. However, such structures resulted in samples with an actual wall thickness of approximately 0.35 mm, independently of the designed one. Another process aspect to be considered is the removal of the sintered or loose powder after production. The capability to remove the powder is strictly related to the pore dimension inside the structure, structure size and waviness of the channel [30]. These features pose a limitation on the minimum unit cell size and the maximum structure size. As an example, in the case of gyroid structures with a cubic cell size of 3.14 mm and a cubic structure with a side of 15.7 mm, Khrapov et al. [23] showed the presence of partially sintered powder trapped inside the structure after cleaning with a sand blasting operation.

Behind the geometrical design and process constraints, considering the common applications, lattice structures are mostly tested under a compression load [8]. However, the tests are performed by adapting the existing standard because no standards are available for the compressive characterisation of lattice structures produced with AM techniques. Commonly, the most adopted standard [23, 24, 27, 31–33] in this field is the ISO 13314:2011 [34], which was originally proposed for stochastic cellular materials. Under compression, the mechanical behaviour of a lattice structure when loaded under a quasi-static compressive load is typically characterised by an initial linear elastic region, followed by a plateau regime with the progressive failure of the struts or surfaces along the failure directions, generally dictated by the geometry of the structure. Besides, the elastic properties obtained from the linear section of the compression curve, the compression test allows an evaluation of the capability to absorb energy and the energy absorption efficiency of the considered structure [35]. The mechanical behaviour of lattice structures is influenced by several factors, such as the material, the relative density, the geometry of the base cell and the eventual post treatments [8]. However, commonly, the relative density is the only parameter used to describe the dependency of mechanical properties. For surface-based structures, the wall thickness plays a central role in the mechanical response. As mentioned above, these structures are usually designed with a constant wall thickness. However, examples are available in the literature in which the thickness or the relative density of the structure is varied along the structure [36]. Such a thickness variation is usually referred to as grading, and it is applied to the TPMS structures smoothly without the introduction of sharp thickness variations of the geometry [21]. When the grading is driven by a functional requirement for the structure, these structures are usually identified as functionally graded lattices (FGL) or density graded lattices (DGL) [37]. However, this term is often used improperly because, in most cases, the structure is designed a priori without any load driven analyses and with the aim only to explore the effect of a certain grading direction on the mechanical behaviour of the structure. The works in this direction are growing because it is a feasible manner to tune the mechanical properties of the structure [21, 31, 35, 38–43]. However, these works consider the thickness variation only along one preferential direction [21, 31, 35, 39–43]: (a) aligned to the larger dimension of the sample [21, 31, 35, 39–43]; (b) Radial from one edge of the sample [43], (c) radially in planes coincident with the cross section of the sample [31] or (d) radially in the three dimensions from the centre of the sample [38]. Depending on the considered gradation and geometry, the samples may show a collapse along the load direction [35, 41], barrelling deformation [31, 38, 42], lateral expansion of the structure at the load application points [39, 42, 43], and shear rupture diagonal with respect to the load direction [31, 38]. The graded structures, with a smaller relative density with respect to the non-graded structures, show a reduced value of stiffness and mechanical properties [42]. The next level of complexity is grading the thickness of the structure in multiple directions in the 3D space.

This paper covers this literature gap, advancing the characterisation of such structures with multiple grading patterns. Focusing on the gyroid structure, this work explores different ordered grading patterns, each oriented along multiple directions, resulting in a fully three-dimensional gradation. Samples were produced using the PBF-EB process, characterised by computed tomography (CT) scanning, and tested under compression. This combined analysis serves, first, to preliminarily assess the impact of the manufacturing process on the final structure, and second, to correlate the mechanical properties with the actual morphological features. In addition, digital image correlation (DIC) is employed to investigate how the grading pattern influences the deformation modes of the structure.

## 2 Methodology

### 2.1 Design of the structure

This work focused on the gyroid TPMS structure. The design process started from the definition of a unitary cell. The gyroid surface is described by elliptical integrals that parametrise the structures in the three spatial directions [44]. In this work, however, a simplified form was considered and the gyroid was designed based on the level-set approximation [45–47], which considers the leading terms of the Fourier series describing a nodal surface as proposed by Klinowski et al. [48]. Considering the x, y and z directions, Eq. 1 reports the level-set approximation equation adopted in this work to describe the gyroid:

$$\begin{aligned}\Phi(\mathrm{x},\ \mathrm{y},\ \mathrm{z}) = {} & \sin\left(\frac{2\pi}{L_x}\mathrm{x}\right)\cos\left(\frac{2\pi}{L_y}\mathrm{y}\right) \\ & + \sin\left(\frac{2\pi}{L_y}\mathrm{y}\right)\cos\left(\frac{2\pi}{L_z}\mathrm{z}\right) \\ & + \sin\left(\frac{2\pi}{L_z}\mathrm{z}\right)\cos\left(\frac{2\pi}{L_x}\mathrm{x}\right) = \mathrm{t}(\mathrm{x},\mathrm{y},\mathrm{z})\end{aligned} \tag{1}$$

where t(x,y,z) is a level-set constant or thickness parameter which controls the offset from the minimal surface. This is a function of the three spatial directions. The value of t determines the volume of the structure as the material enclosed between two surfaces obtained by choosing ± t, which are the offsets of the base surface. Changing the value of t in the space of the structures produces the thickness gradation [49]. $L_x$, $L_y$ and $L_z$ are the dimensions of the unitary cell in the x, y and z directions, respectively.

The structures were designed using the software nTop (nTopology, New York, United States). This software allowed a fast and straightforward parametric design of the structures. Figure 1 a) shows the unitary cell selected in this work. This has a dimension of 10 × 10 × 10 mm. Figure 1 a) also shows the longitudinal and traverse surfaces (highlighted in orange and light blue, respectively) that are the cross-section of the structure at the unitary cell boundary. The unitary cell was repeated in an ordered manner within a volume of dimensions equal to 20 × 20 × 30 mm. Therefore, two cells are present along the x direction, two cells along the y direction and three cells along the z direction, for a total of 12 cells (Fig. 1b)). The z-axis is aligned to the build direction.

As discussed in the introduction section, the size of the unitary cell and the overall size of the structure were chosen to ensure the possibility of removing all the sintered powder from the structure and to ensure the feasibility of the structure. The minimum wall thickness was chosen to be large enough to be far from the minimum electron beam diameter [50] and subsequently to limit the effect of the beam diameter on the wall thickness. The structures with constant wall thickness were designed with a uniform value of either 0.7 mm (referred to as “minimum thickness” or $t_{min}$) or 1.4 mm (referred to as “maximum thickness” or $t_{max}$). These served as reference cases for comparing the subsequent 3D variations in thickness between the selected minimum and maximum values (Fig. 2). Each graded structure is generated by first defining the position of the so-called initiator surface, which is a 2D or 3D surface intersecting the cuboidal volume of the sample. The location of this surface determines the cross-section where the thickness is initially assigned, and from which the thickness grading begins. Therefore, at the intersection between the initiator surface and the sample volume, the thickness is set to either $t_{min}$ or $t_{max}$. From this surface,

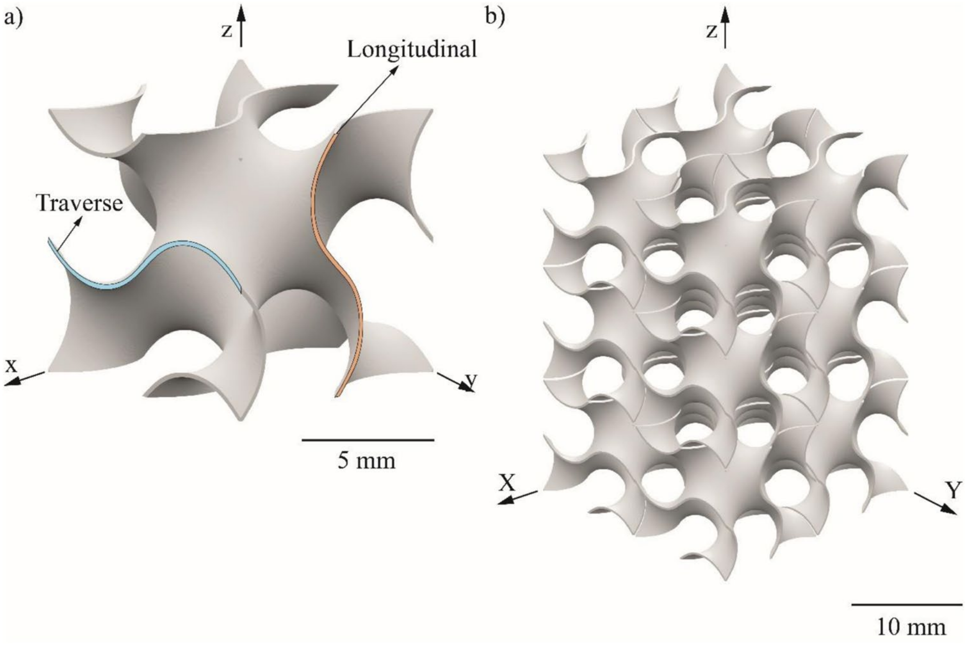

**Fig. 1** **a** Gyroid unitary cell, with highlighted in orange the surface longitudinal to the build and load direction and in light blue the surface traverse to the build or load direction. **b** Repetition of the cell in the space

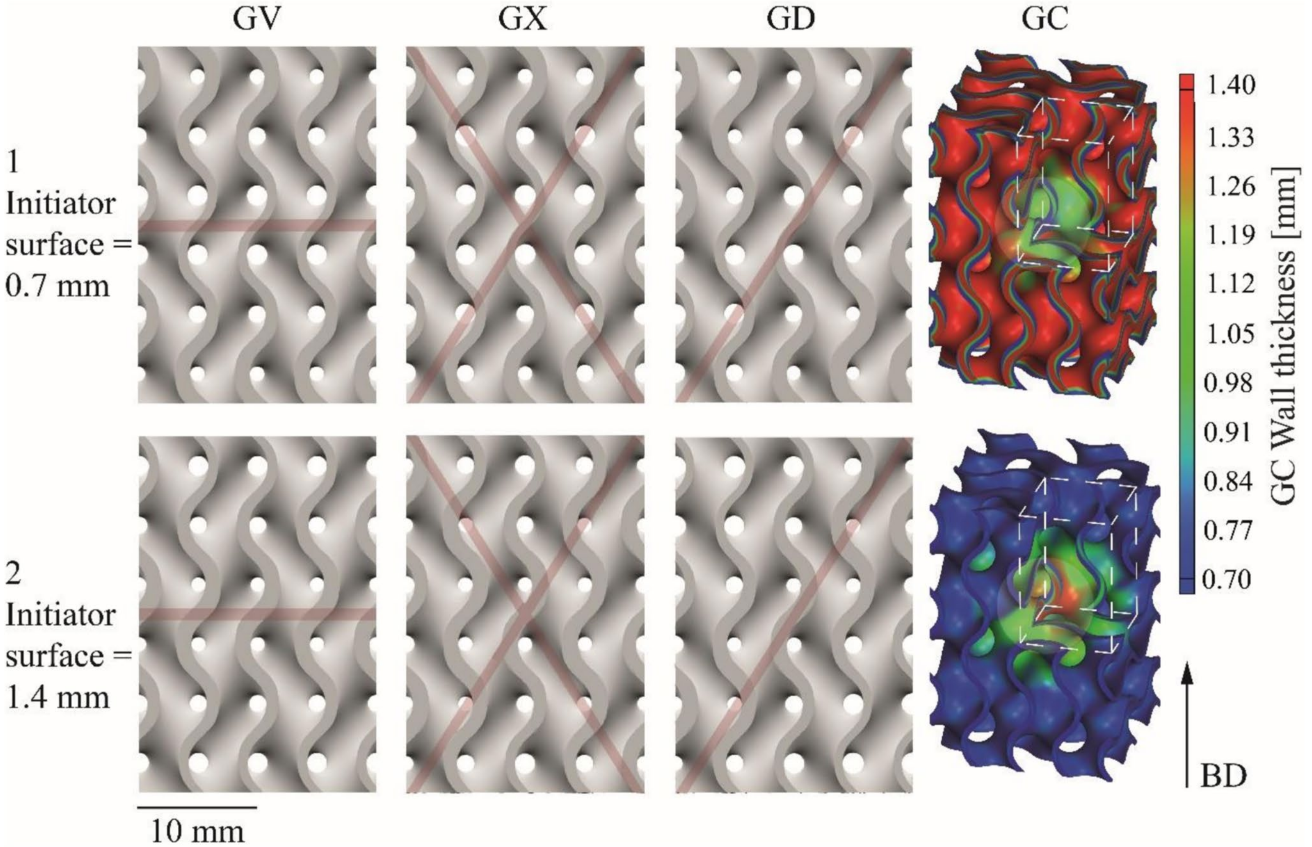

**Fig. 2** Grading pattern in the space of the structures. For GV, GX and GD structures, the initiator surface is a plane positioned orthogonal to the figure plane and highlighted with a red line. For the GC structure, the initiator surface is the external surface of a sphere centred at the centre of gravity of the cuboid, as visible in the 3D isometric view with cross-sectional cuts and the wall thickness map is shown. The thickness of the initiator surface is out of scale. BD is the build direction

the thickness is linearly graded—either normally or radially—until it reaches the opposite extreme value ($t_{max}$ or $t_{min}$). Therefore, for each initiator surface, two structures are designed. The 2D initiator surface is defined as either a horizontal or a diagonal plane, while the 3D initiator surface can be either a spherical surface centred within the sample or a cross-shaped surface formed by the intersection of two diagonal planes. Each configuration is labelled with the prefix G, followed by a letter indicating the type of initiator surface, and a number representing the thickness assigned along the initiator surface. Additionally, the use of the number allows for immediate distinction of the structures into two groups: group G1 collects all the structures with a thickness of the initiator surface of 0.7 mm. Group G2 includes all the structures with a thickness of the initiator surface of 1.4 mm.

Figure 2 shows the thickness-graded samples considered in this work. These are the following:

- Uniform thickness, UT refers to the structures with a constant wall thickness. Two structures were considered GUT1 and GUT2. For these structures, the nominal relative density varied between 19.6 and 39.2%, respectively.
- Vertical, V indicates the structures in which the initiator surface is the middle plane perpendicular to the build direction. Therefore, the wall thickness was varied linearly and perpendicularly to the middle horizontal plane in both directions. This gradation is the same in the thickness of the structure (orthogonally to the side view shown in Fig. 2). Two variants of the structure were considered: GV1 and GV2. For GV1, the initiator surface had a thickness of 0.7 mm, and the structure had a relative density of 29.0%. GV2 is designed with an initiator surface of 1.4 mm, and the structure has a relative density of 29.7%.
- Diagonal, D indicates the structures in which the initiator surface lies on the diagonal plane of the parallelepiped with the normal tilted 45 degrees counterclockwise from the build direction. This gradation pattern does not change in the planes parallel to the side view shown in Fig. 2. Therefore, the wall thickness was varied linearly and perpendicularly to the diagonal plane in both directions. The considered structures were GD1 and GD2. GD1 has a diagonal initiator surface with a thickness of 0.7 mm, and the structure has a relative density of 30.3%. GD2 is designed with a diagonal initiator surface with a thickness of 1.4 mm and a relative density of 28.4%.
- Cross, X indicates the structures for which the initiator surface is a cross-shaped surface formed by the intersection of the two diagonal planes tilted from the build direction 45 degrees clockwise and counterclockwise, respectively. The wall thickness is therefore varied perpendicularly to the initiator surface. This gradation is the same in all the planes parallel to the side views shown in Fig. 2. The structures considered were: GX1 and GX2. GX1 has two intersecting surfaces of 0.7 mm and a relative density of 24.6%. GX2 has two intersecting surfaces of 1.4 mm and a relative density of 32.9%.
- Core, C indicates the structures in which the initiator surface is spherical with a diameter equal to 17 mm and positioned at the centre of gravity of the parallelepiped structures. For this structure, the wall thickness is varied linearly toward the centre of the sphere, while, toward the outside of the structure, the thickness is assumed constant and equal to the thickness assigned at the initiator surface. Figure 2 shows a 3D view of this structure, with a section showing the core of the structure. In addition, a wall thickness map is displayed to clarify the wall thickness gradation pattern. Two structures were considered: GC1 and GC2. GC1 has a thickness from the initiator surface toward the outside of 0.7 mm, resulting in a relative density of 37.4%. GC2 is characterised by an initial core wall thickness of 1.4 mm from the initiator surface toward the outside and a relative density of 21.5%.

## 2.2 Production

The samples designed in the nTop environment were exported as Parasolid models and converted in STL. The build preparation was conducted using Magics (Materialise, Leuven, Belgium). The samples were produced using the PBF-EB machine Arcam A2X (Colibrium additive a GE aerospace company, Mölnlycke, Sweden). The material adopted was the Ti6Al4V. Table 1 reports the process

**Table 1** Process parameters adopted for contour with multibeam strategy and hatch

| Melting strategy | Scan speed [mm/s] | Focus offset [mA] | Beam current [mA] | Number of spots | Number of contours | Hatch contours [mm] |
|---|---|---|---|---|---|---|
| Multibeam | 850 | 6 | 5 | 70 | 3 | 0.29 |
| Melting strategy | Speed function [mm/s] | Focus offset [mA] | Beam current max [mA] | Reference length [mm] | Reference current [mA] | Line offset [mm] |
| Hatch | 45 | 25 | 20 | 45 | 12 | 0.2 |

parameters adopted for the production. The cross section was melted in two steps: the contour with Multibeam™ and hatch. For the sake of statistics, three replicas were produced for each geometry, with a total of 30 samples produced in one build. The samples were produced directly attached to the start plate. As reported in Sect. 2.1, samples were produced with the build direction aligned to the z-axis shown in Fig. 1. Samples were rotated by 45° around the z-axis and evenly distributed on the start plate with a minimum distance among the samples of 8 mm to avoid heat interaction. To avoid systematic effects, the position of the samples on the start plate was randomised.

After the production, the samples were cleaned with a sandblasting process using the Arcam powder recovery system (PRS) and the same powder used in the process.

## 2.3 Morphological characterisation

One sample for each geometry was inspected using a computed tomography scanning (CT-scan) system, GE phoenix V| tome|x s (GE inspection technologies, Wunstorf, Germany). CT-scans were performed with a voltage of 140 kV and a current of 170 µA. The adopted voxel size, which defines the resolution of the tomography, was approximately 35 µm. This voxel size allowed for capturing the complete sample. 1001 tomograms were acquired for each sample. The tomograms were elaborated using the software VGStudio Max 3.4 (Volume Graphics GmbH, Heidelberg, Germany). This software was adopted to perform the following analyses:

- Surface determination of the structure. This is a preliminary step required to distinguish the solid material from the background clearly. Once the surface of the structure is defined, it is possible to calculate the volume of the structure by counting the number of voxels identified as solid material.
- Extended Porosity/Inclusion analysis. This analysis allowed the evaluation of the presence of porosities in the bulk regions of the samples. The output of this analysis is the volume of the internal enclosed porosities expressed in $mm^3$.
- The Wall Thickness Analysis. This analysis uses the sphere method to evaluate the thickness distribution of the structure. The output of this analysis is a histogram of the wall thickness occurrences. The wall thickness analysis was also performed for the nominal geometry, and this allowed a comparison between the produced geometry and the nominal geometry. The comparison was made by comparing the highest peaks in the wall thickness distributions for the produced and the nominal structure.
- The Nominal/Actual Comparison. This analysis allowed the evaluation of the dimensional accuracy of the structure as reconstructed from tomography in comparison with the nominal STL file. The alignment between the produced geometry and the nominal was performed using the algorithm of best-fit registration. The outcome of this analysis is a distribution of the frequency of the relative dimensional deviations identified in the samples available, also in the cumulative form.

## 2.4 Mechanical characterisation

Quasi-static uniaxial compression tests were performed to characterise the mechanical properties and the deformation behaviour under compression loads using a universal testing machine Easydur Aura 10T (Easydur Srl, Arcisate, Italy), with a 100 kN load cell. As mentioned in Sect. 1, no standards are available for the testing of micro-architectured geometries produced with additive manufacturing techniques. Therefore, in this case, tests were performed according to the ISO 13314:2011 [34] using a displacement rate of the crosshead of 2 mm/min. Stress values were calculated as the ratio of the measured applied load divided by the envelope cross-section area of the lattice structures. The failure strain was set at 50% of the specimen height. Results for the quasi-elastic gradient (E) [35], first maximum compressive strength (FMCS), compressive offset stress ($\sigma_c$), plateau stress ($\sigma_{pl}$) and energy absorption at 50% strain ($W_{50}$) were calculated following ISO 13314:2011 standard [34]. The $\sigma_{pl}$ was evaluated considering the strain that goes from 20 to 40%. The ductility characteristics of the structures were evaluated from the magnitude of the energy absorption ($W_v$) and the energy absorption efficiency ($\eta$). $W_v$ was calculated using Eq. (2) and is given as the area subtended to the stress–strain curve within the maximum strain of the structure ($\varepsilon_f$) [51]. For the current work, the considered maximum deformation was $\varepsilon_f = 50\%$. In this case, $W_v$ can be identified as $W_{50}$. Equation (3) shows the computation of energy absorption efficiency $\eta(\varepsilon)$. This is defined as the absorbed energy under any strain divided by the corresponding stress $\sigma(\varepsilon)$ [52]. For the current work, $\eta(\varepsilon)$ was evaluated considering $\varepsilon_f = 50\%$

$$W_v = \int_0^{\varepsilon_f} \sigma(\varepsilon) d\varepsilon \tag{2}$$

$$\eta(\varepsilon) = \frac{1}{\sigma(\varepsilon)} \int_0^{\varepsilon_f} \sigma(\varepsilon) d\varepsilon \tag{3}$$

Besides the values suggested by the ISO 13314:2011, the Specific energy absorption (SEA) was evaluated from the data obtained from the compression test. This was calculated by normalising the absorbed energy up to 50% strain ($W_{50}$) with the product of the relative density of the structure and the bulk density of the base material. The SEA is calculated according to Eq. 4:

$$\mathrm{SEA} = \frac{W_{50}}{\rho_{\mathrm{rel}} \times \rho_{\mathrm{bulk}}} \tag{4}$$

where $W_{50}$ is the energy absorbed per unit volume up to 50% strain, $\rho_{rel}$ is the relative density of the graded structure, and $\rho_{bulk}$ is the bulk density of Ti6Al4V (4.43 g/cm$^3$ [53]). This formulation allows for a direct comparison of energy absorption efficiency across structures with varying material distributions. The compression test was conducted for each sample, with a total of 30 compression tests.

## 2.5 Digital image correlation analysis

Digital image correlation (DIC) enables a qualitative and quantitative analysis of the behaviour of the material under mechanical load. In this work, the 2D-DIC method was employed during the compression test to investigate the deformation patterns and failure mechanisms of one sample for each of the considered structures, analysing the strain field distributions at a part-scale level. Following a methodology proposed in literature [54, 55], no speckle pattern was applied, as the surface roughness inherent to the EB-PBF process and the light reflection were utilised as a natural speckle pattern for tracking deformations. The Ncorr toolbox [56] for MATLAB was utilised to perform the DIC analysis. This enables the determination of the displacement and strain fields within a region of interest (ROI) of the sample through image processing techniques. The images captured during the deformation are processed to establish a one-to-one correspondence between material points in the initial undeformed state and subsequent deformed stages. To obtain the highest reliability of the results, it is important to consider a few potential sources of error and minor limitations when conducting DIC with this method. Firstly, the 2D DIC analysis on lattice specimens may introduce some errors in out-of-plane regions, especially during deformation. Additionally, variations in light reflection during deformation may slightly alter the speckle pattern, which could introduce measurement errors. This is particularly relevant for surfaces with high roughness, where changes in reflection during the deformation can impact the contrast and visibility of the speckle pattern. To address these issues, the region of interest (ROI) has been defined prior to DIC analysis on the final deformed image using a backwards analysis approach. This approach ensured that regions subjected to folding or shadowing during deformation were excluded from the ROI, preventing the camera from losing sight of portions of the speckle pattern. The local tensile/compressive strains calculated in the loading direction, referred to as Eulerian strain (ε), are selected for visualising and comparing the different deformation modes of the structures. As shown in Fig. 3, the DIC reference images of the samples were analysed by a Matlab user script to assess the quality of the speckle pattern, computing the mean equivalent speckle diameters, the average minimum distances between the speckles, and the area coverage, defined as the percentage ratio between the area of the speckle pattern and the total area considered (speckle + background). The cumulative percentage plot of the speckle equivalent diameter is reported in Fig. 3 with a

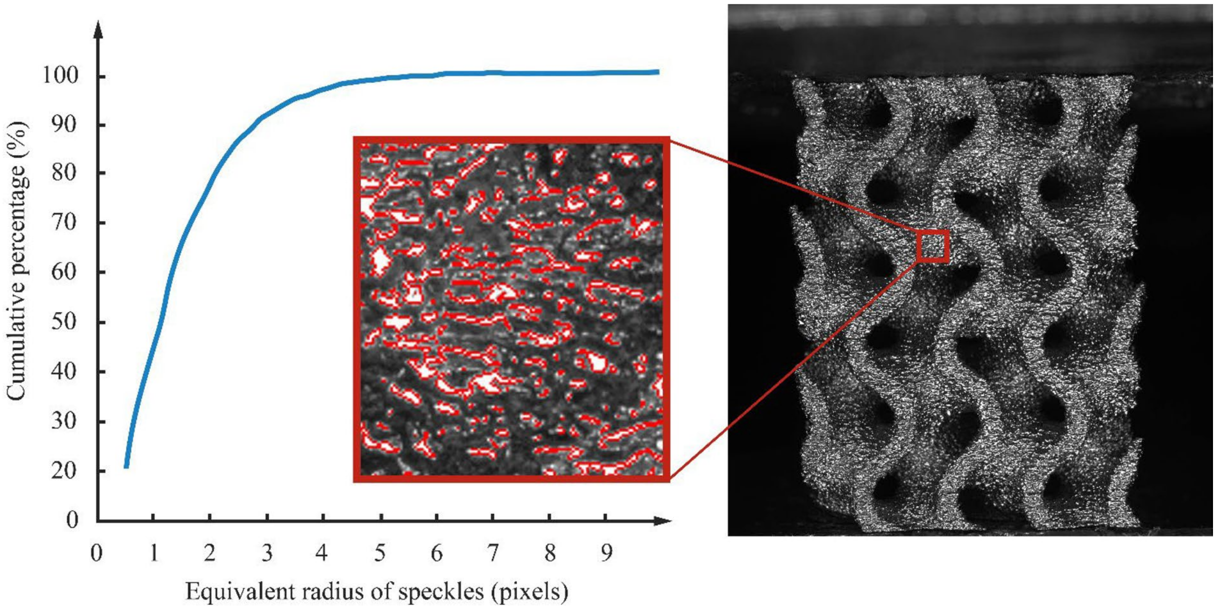

**Fig. 3** Speckle pattern characterisation

magnification of the analysed speckle pattern. It resulted in mean equivalent speckle diameters of 3.09 ± 2.13 pixels and average minimum distances between speckles of 6.17 ± 2.64 pixels. According to the guidelines provided by the International Digital Image Correlation Society (iDICs) [57], these results indicate a good quality speckle pattern, as the speckle sizes fall within the 3–5 pixel optimal range for accurate DIC measurements [57, 58]. Having achieved a resultant area coverage of 20%, a subset radius of 12 pixels was utilised for the DIC analysis, providing the best correlation coefficients and a good compromise in strain resolutions. Larger subsets typically result in lower displacement noise, but often at the cost of increased spatial smoothing. The choice of 12 pixels for the subset radius ensured robust and accurate measurements, enabling the correct identification of regions with the highest deformations. It is also worth noting that, since these are part-scale DIC analyses, the focus was not on achieving the highest accuracy in strain measurement but instead on capturing the deformation patterns of the structures.

To compare the different structures, the strain plots calculated from the DIC analyses are discussed in the results section, considering three significant stages of deformation for each specimen type. Specifically, the first stage is chosen in the linear region of the compression load response, corresponding to a global strain of 0.02 ($\varepsilon_{0.02}$), to observe how small compression loads are distributed within the structure. The other two stages correspond to the occurrence of the compressive offset stress ($\varepsilon_{\sigma c}$) and the first maximum compressive strength ($\varepsilon_{FMCS}$), to analyse the behaviour of the structures when subjected to distributed plasticity and subsequently to structural instabilities originating at the FMCS.

# 3 Results

## 3.1 Morphological characterisation

Figure 4 shows the results for relative density, volume deviation and internal enclosed porosity, arranged according to actual relative densities. Overall, the material of the structure resulted in being homogeneous with a limited number of enclosed porosities characterised by a small volume. As an example, Fig. 5 shows the result for the GC2 structure. The porosity size is represented in a coloured map, in which the warm colours refer to pore size with higher volume. The pores were overall extremely small, and the density of the solid material was always above 99.99% (Fig. 4, porosity below 0.0025%). For this level of density, the solid fraction of the structures can be considered as fully dense [59]. The results of porosity analysis show that the enclosed porosities decreased as the relative density of the structure increased. The lowest level of porosity, 0.0005% was found for the sample GUT2, the structure with the highest relative density. On the other hand, the samples with the lowest relative density, such as the GUT1 or the GC2, were characterised by a higher level of porosity, which for the GC2 sample was equal to 0.0023%.

As concerns the geometrical characteristics, the fabricated samples were found to be smaller than the nominal geometry. This result can be explained by the fact that no geometrical correction has been applied to the nominal geometry to compensate for the volume shrinkage during the cooling phase. The evaluation of such shrinkage on thin walls, including also the variation of thicknesses in the structure, is a challenge and varies among the structures and in

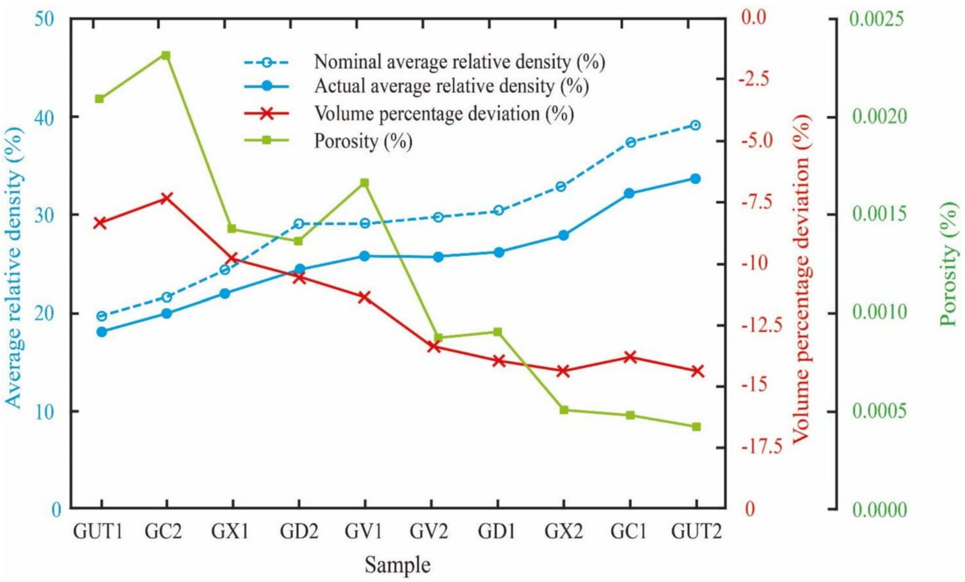

**Fig. 4** Results of the average nominal/actual relative densities, actual volume percentage differences from nominal STL and porosity of the samples

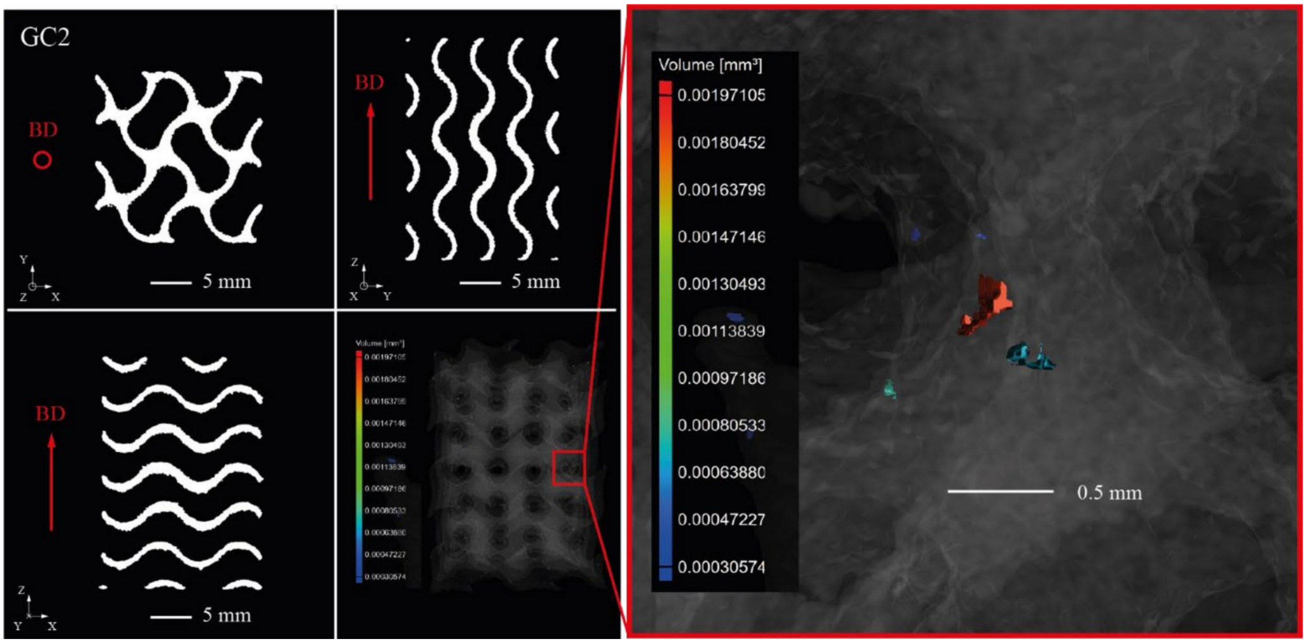

**Fig. 5** Example of tomograms for the structure GC2 and classification of the identified porosities according to the volume

the different thicknesses. In fact, the volume of the produced structures, compared to the nominal volume, exhibits an increasing percentage deviation as the average relative density and corresponding thicknesses increase, ranging from approximately −5% of the GC2 to −15% of the GUT2. As for the volume, the same trend is observed in the relative densities of the produced structures, consistently displaying lower values compared to the nominal ones, with increasing percentage differences ranging from −7.4% for GC2 to −14.4% for GX2, as shown in Fig. 4.

The results regarding the volume and the relative density of the fabricated sample can also be discussed considering the actual wall thickness of the structures. Figure 6 illustrates the comparisons between the wall thickness distributions calculated for the reference STL and those calculated from CT-scan reconstructions. The peaks in Fig. 6 correspond to the most frequent thickness in the structure, thus providing a reliable basis for a global comparison between the nominal and actual geometries. As can be observed, for all the structures, the wall thickness is always slightly shifted to the left of the wall thickness distribution obtained for the nominal geometry. This means that the characteristic thickness of the structures is always globally smaller than the designed one. Compared to the STL distributions (black line in Fig. 6), the produced structures exhibited a broader variation in thickness (larger variance and lower mean), with long tails in the measured distributions showing areas of the structures which are larger than the designed ones (positively skewed). These tails are indicative of localised increases in wall thickness, primarily due, as mentioned above, to the surface roughness of the samples, characterised by the presence of powder particles partially sintered on the surface of the structure and not removed during the sandblasting process with PRS. This phenomenon is well documented in the literature. In areas of the samples that present downskin surfaces built on unmelted material, the heat dissipation is less efficient, favouring the sintering and partial melting of powder particles on the surface [60].

In the case of the reference structures with a uniform thickness, the actual thickness of the structure exhibited a peak close, but smaller than, the designed thickness (0.7 mm for the GUT1 and 1.4 mm for the GUT2). The graded structures present a distribution of less prominent peaks, associated with the intermediate thicknesses between the minimum and maximum values. The differences in thickness between the fabricated and the STL design are also confirmed by the Nominal/Actual comparison, as shown in Fig. 7. The relative deviations and the cumulative deviations distributions obtained from the nominal/actual for all the samples comparison overlaps, with the graded samples that are included between the uniform thickness samples GUT1 and GUT2. GUT1 displayed a peak value at –0.153 mm, positioned on the right of the distribution, while the denser GUT2 had a peak at – 0.557 mm, placed on the left of the distribution. This result can be interpreted as a systematic error or a signature of the process. The difference between the nominal and the actual wall thickness distribution was found to grow according to the relative density of the structure. For example, GUT1, which is the structure with the lowest

**Fig. 6** Wall thickness analysis results of the comparison between the distributions of the nominal STL geometries and the distributions obtained from CT-scans

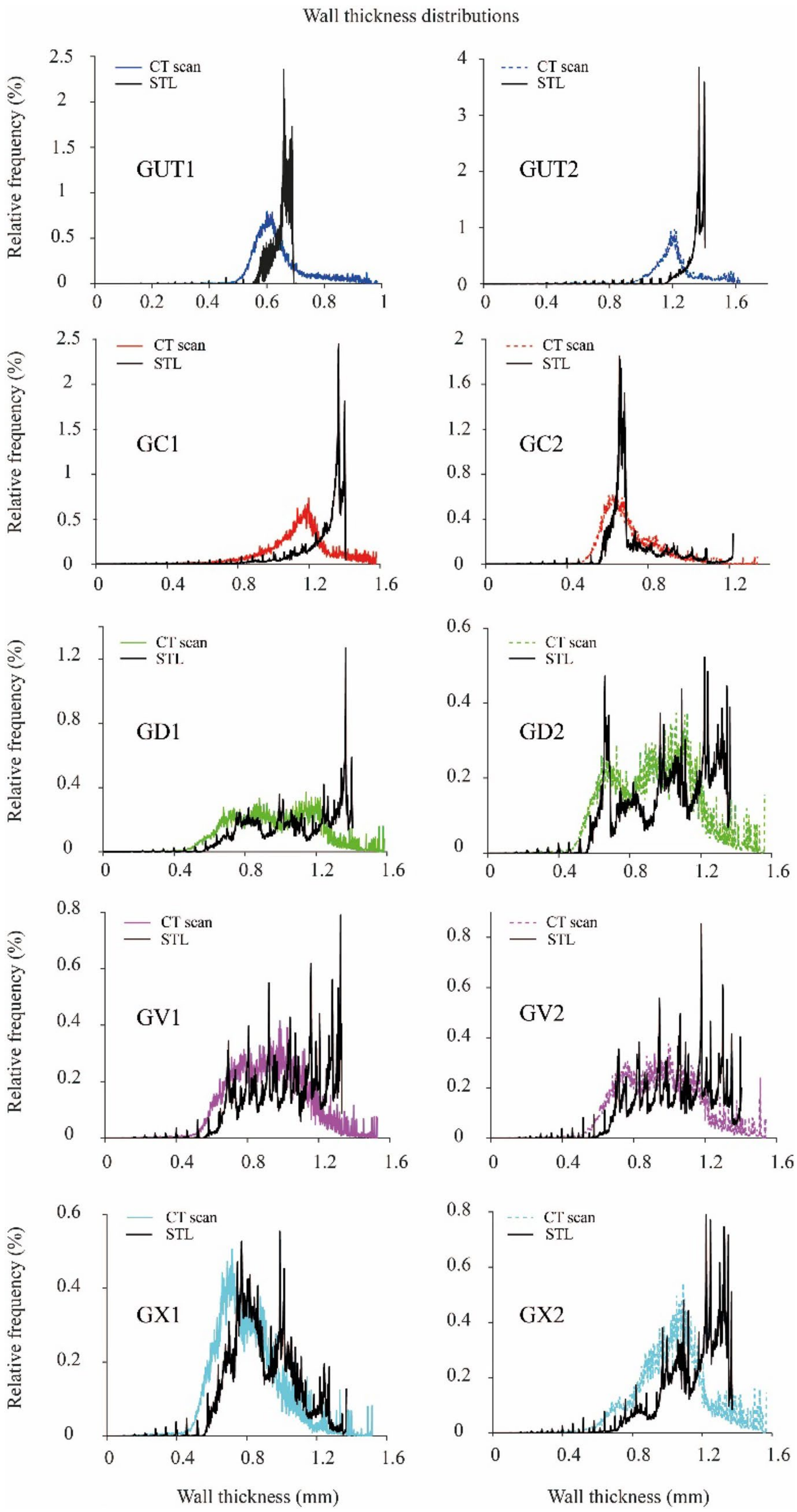

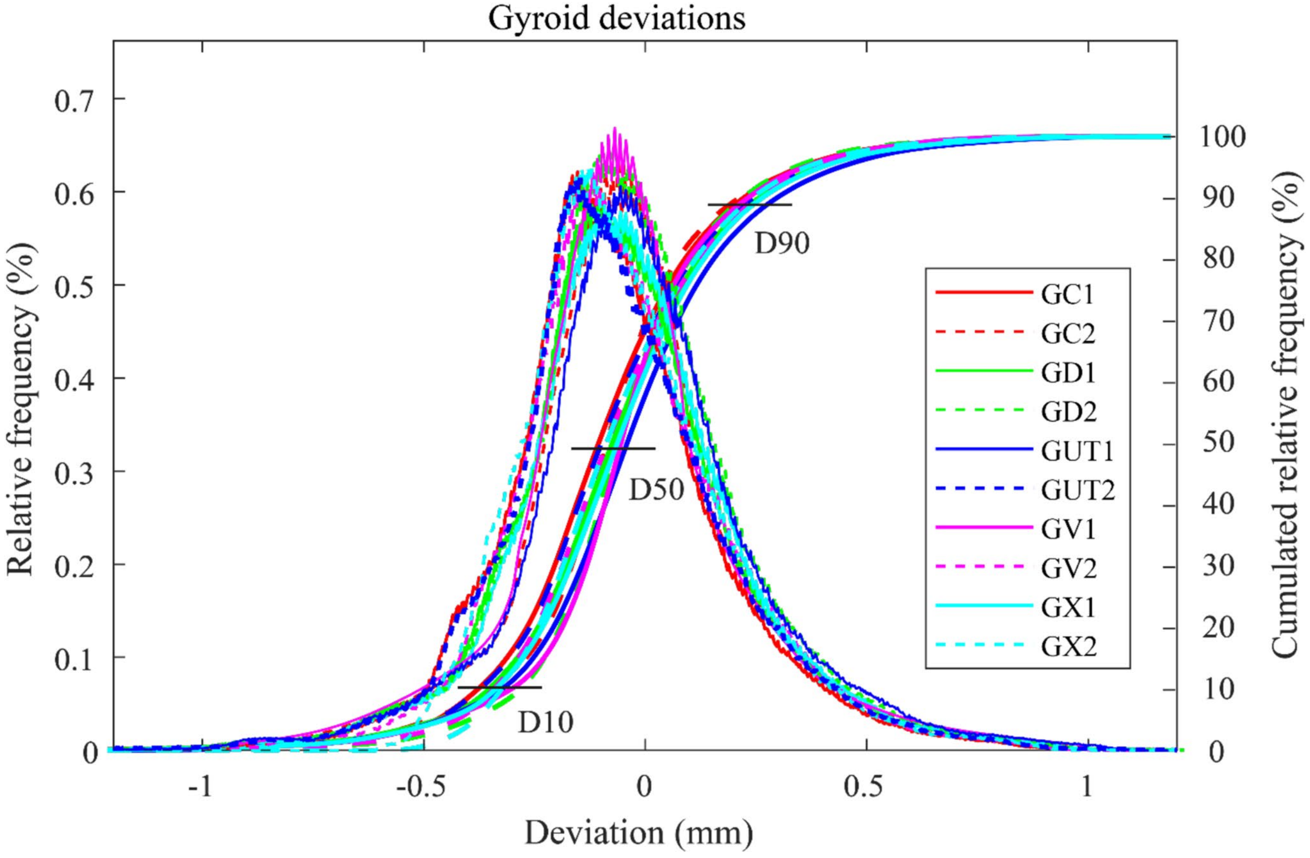

**Fig. 7** Relative deviations and cumulative deviations obtained from the nominal/Actual comparison analysis for the gyroid structures considered in this work

relative density, exhibits a distribution of the actual wall thicknesses with a peak that is approximately 8% lower than the nominal distribution, which is consistent with the observed volumetric deviation (Fig. 4). GUT2, the structure with the highest relative density, resulted in a deviation between the nominal and the actual thickness of approximately 14%. The core (GC) and cross (GX) gradations showed a similar behaviour to that observed in the structures with uniform thickness. At higher densities, such as GX2 and GC1, higher discrepancies are observed in the deviation between the actual and nominal compared to those found in specimens with lower thicknesses, like GC2 and GX1.

Considering the relative density and the actual morphology of the structure, it is possible to classify the produced structures into two groups. The structures with lower relative densities, such as GC2 and GX1, show a distribution located around the peak deviation of GUT1. In contrast, the structures with higher relative density, such as GX2 and GC1, displayed a peak of distribution comparable to GUT2. In general, negative deviations are more pronounced at higher densities, thus at higher thicknesses. Consequently, even the cumulative deviations (Fig. 7) are near one another, with GUT1 and GUT2 situated at the right and left extremes, respectively. Intermediate values are assumed by the graded structures. The cumulative deviation of all the samples produced, considered in an aggregate form, is characterised by a $D10 = -0.336 \pm 0.047$ mm, $D50 = -0.065 \pm 0.022$ mm, and $D90 = 0.230 \pm 0.077$ mm. The value of the D50 obtained confirms the slight shift to the left obtained for the wall thickness analysis shown in Fig. 6 and discussed above, which could be relative to a shrinkage of the surface as a function of the relative density of the structure.

As a final consideration, Fig. 8 shows as an example the results of the wall thickness analysis for the fabricated GX2 (Fig. 8a)), the nominal/actual 3D comparison (Fig. 8b)) and an overlap in a central section between an actual cross section of the sample and the corresponding nominal section (Fig. 8c)). As can be observed, the highest thickness can be detected along the initiation surface (around 1.4 mm, red in the colour map in Fig. 8a), which rapidly decreases to the minimum thickness (green in the colour map in Fig. 8a). The dimensional deviation from the nominal one is small (Fig. 8b)), except at the base of the sample. In that area, the deviation is larger because the sample was built directly attached to the stainless-steel start plate. This placement

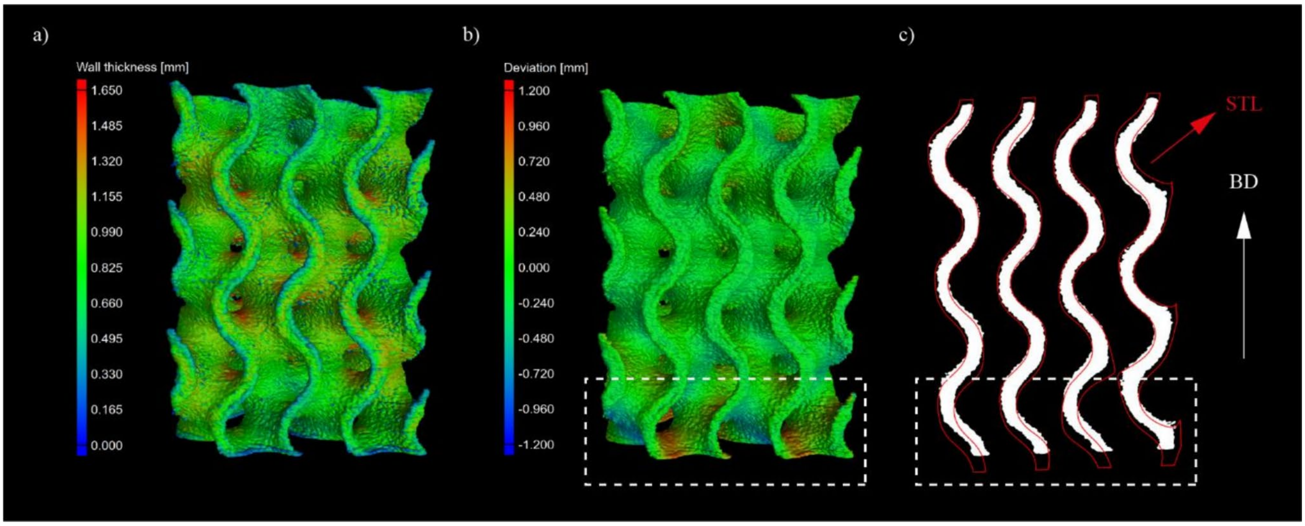

**Fig. 8** GX2 **a** Wall thickness and **b** Nominal/Actual comparison analysis colour maps. **c** STL and actual CT-scan reconstruction superposition

may have a thermal effect on the initial construction of the sample and subsequent cooling and shrinkage [61, 62]. The influence of the start plate may result in thermal-induced deformation, such as in the case of the positive deviation of the geometry or in the slight warping of the deposited layer in the area of the sample perpendicular to the build direction that leads to the negative deviation of the geometry [63]. The measured height of the specimen resulted, therefore, consistently smaller than the nominal 30 mm (Fig. 8c)), ranging from 28.06 mm of sample GUT2 to 28.76 mm of sample GX2, indicating geometric deformations that occurred along the build axis, as noticeable in the superposition of the STL/Actual geometries shown in Fig. 8c). Also in this case, this deviation may be related to thermal inhomogeneities of the process due to non-uniform temperature distribution along the build direction close to the start plate [64].

## 3.2 Deformation mechanisms and mechanical properties

Figure 9 shows the stress–strain curves obtained as an average of the data from the compression test conducted on the three replicas of each geometry. Table 2, instead, reports the average values and the relative standard deviation for mechanical indexes calculated following the ISO 13314:2011 standard on the three replicas.

In agreement with the literature [65, 66] and based on the relative densities of the structures, the curves of the graded structures lie between the curves of the reference uniform thickness structures (GU), with GUT1 and GUT2 as lower and upper limits, respectively. For these two structures, Fig. 10 shows the corresponding Eulerian strain fields calculated along the compression axis obtained from DIC analyses. Negative values indicate compressive strains, while positive values indicate tensile strains. In the colour map in Fig. 10, the compressive strains are represented in blue, while tensile strains, typically of lower magnitude, are shown in red. The presence of tensile strains in the loading (compressive) direction arises from the local bending and flexural deformation of the wall surfaces in the TPMS geometries. This phenomenon is a result of the complex stress redistribution that occurs during compression, particularly in regions where the geometry promotes localised curvature or instability. Compared to GUT2, GUT1 displayed a less uniform distribution of strain across the analysed area. GUT1 is characterised by more concentrated local strains, both tensile and compressive, especially in the walls aligned with the load direction (longitudinal surface highlighted in Fig. 1), as highlighted by the dashed boxes in Fig. 10. This behaviour is consistent with the findings in the literature [18, 22, 30, 32, 67, 68]. The surfaces with higher curvature near the channels are subjected to tensile deformations (traverse surfaces in Fig. 1, dashed boxes in Fig. 10), while the parts of the surface aligned with the load direction are under compression. The pronounced strain concentration observed along the vertical ligament at $\varepsilon_{\sigma c}$, which exhibits a snake-like geometry as highlighted in Fig. 10, is characterized by steep localized gradients that leads to structural instabilities within the regions delineated by the dashed boxes in Fig. 10, causing the structure to collapse and propagate along diagonal shear bands (red lines in Fig. 12), as previously noted in the literature [22, 27, 32, 68, 69]. In GUT2, a more uniform strain distribution is observed, with lower locally tensile strain values. In proximity to global strains of 0.13 corresponding to the onset

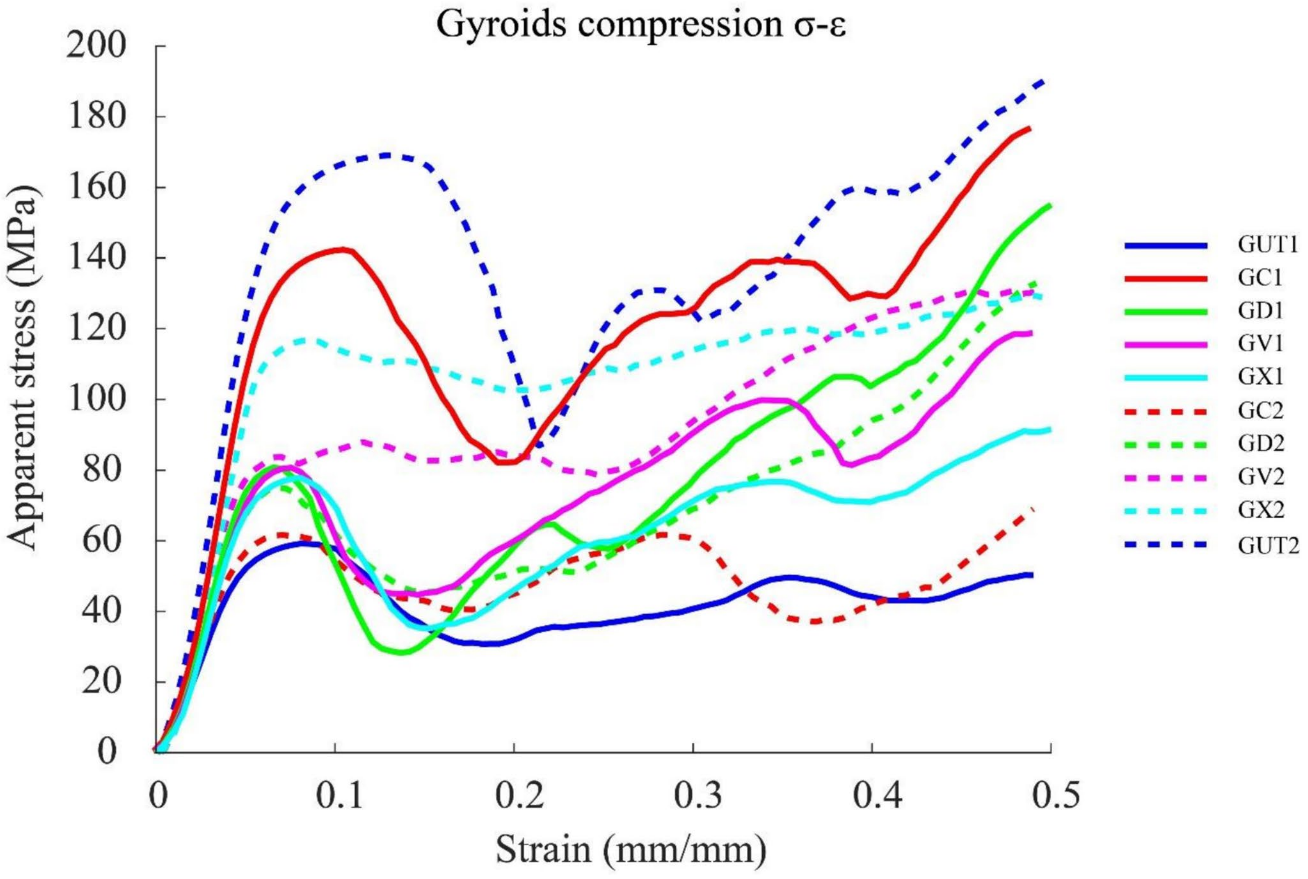

**Fig. 9** Stress–strain plots of the compression tests

**Table 2** ISO 13314:2011 calculated mechanical performance indexes reported as the mean M values and the relative standard deviation SD

| Sample | Quasi elastic gradient [MPa] | | Compressive offset stress ($\sigma_c$) [MPa] | | First maximum compressive strength (FMCS) [MPa] | | Plateau stress ($\sigma_{pl}$) [MPa] | | Absorbed energy ($W_{50}$) [J/mm$^3$] | | Specific Energy absorption SEA [J/kg] | |
|---|---|---|---|---|---|---|---|---|---|---|---|---|
| | M | SD | M | SD | M | SD | M | SD | M | SD | M | SD |
| GUT1 | 1373.2 | 99.1 | 49.2 | 3.3 | 61.9 | 0.8 | 43.5 | 1.5 | 21.9 | 0.5 | 2.8E7 | 5.2E5 |
| GUT2 | 3178.4 | 87.1 | 125.0 | 2.9 | 169.1 | 2.2 | 135.3 | 10.7 | 67.8 | 2.4 | 4.5E7 | 8.0E5 |
| GC2 | 1605.8 | 18.1 | 53.0 | 0.6 | 61.6 | 1.8 | 46.9 | 1.2 | 23.5 | 0.3 | 2.7E7 | 2.9E5 |
| GD2 | 1809.4 | 35.0 | 62.6 | 1.2 | 75.1 | 1.2 | 68.5 | 6.6 | 34.3 | 1.2 | 3.0E7 | 7.9E5 |
| GV2 | 2338.7 | 102.8 | 69.5 | 3.4 | 83.8 | 0.3 | 91.3 | 2.3 | 45.8 | 1.3 | 4.0E7 | 6.4E5 |
| GX2 | 2560.7 | 89.0 | 105.0 | 3.0 | 116.7 | 2.8 | 105.1 | 1.8 | 52.8 | 1.0 | 4.2E7 | 4.3E5 |
| GC1 | 2843.6 | 87.3 | 112.1 | 2.9 | 143.8 | 0.7 | 117.0 | 7.8 | 58.6 | 0.7 | 4.1E7 | 2.7E5 |
| GD1 | 2049.8 | 21.0 | 68.8 | 0.7 | 75.1 | 0.7 | 76.0 | 11.7 | 38.0 | 1.3 | 3.3E7 | 7.7E5 |
| GV1 | 1821.2 | 63.1 | 67.3 | 2.1 | 83.8 | 1.2 | 73.0 | 4.6 | 36.6 | 0.9 | 3.2E7 | 5.6E5 |
| GX1 | 1901.4 | 50.0 | 59.7 | 1.7 | 78.2 | 0.9 | 62.2 | 2.6 | 31.2 | 0.6 | 3.2E7 | 4.3E5 |

of the structure FMCS (169 MPa), the highest compressive strains are distributed over a larger surface area compared to GUT1, particularly in the vertical support walls, with fewer concentrated tensile strains in the channel curvatures, indicating greater deformation capacity. Indeed, the onset of the first instability peak occurs at global strains

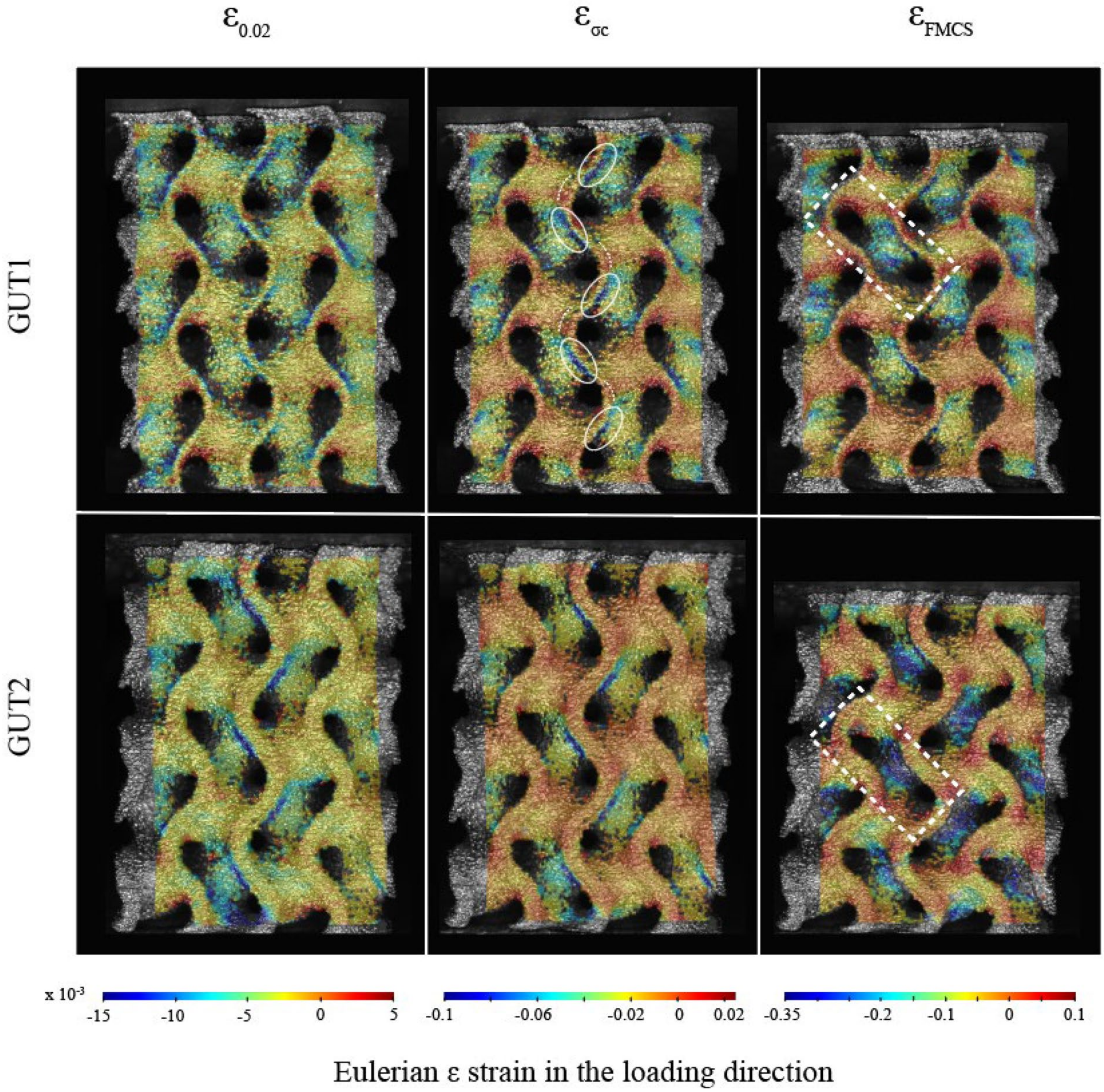

**Fig. 10** Eulerian longitudinal strain obtained from DIC analysis of GUT1 and GUT2 specimens. In blue, the compressive strains, while in red, the traction strains. The snake-like geometry highlighted in GUT1 $\varepsilon_{\sigma c}$ represents the localised steep gradients that occur across the channel regions where the failure starts. The dashed box locates the area where the failure starts

twice those of GUT1 (0.07). After the onset of FMCS in GUT2, a greater peak drop is observed, followed by a steepening of the stress–strain response in the plateau region. In contrast, GUT1 exhibited a plateau region at almost constant load (43.5 MPa). The different behaviour outlined is due to the doubling of the wall thickness and is consistent with the results obtained in literature [8, 65].

Figures 11 and 12 show the Eulerian longitudinal strain and the deformation behaviour with the failure mode of the graded structures considered in this work, respectively. Like in Fig. 10, in Fig. 11, compressive strains are considered as negative (blue in the figure) while the tensile strains are positive (red in the figure). The strain fields obtained from DIC analyses demonstrate that all the structures exhibit similar instability behaviours to those observed in the uniform reference structures. For all the samples, most of the structure is characterised by a compressive strain of modest entity (orange in Fig. 11). However, the images show the presence of zones of tensile strain (red in Fig. 11). The structural collapse, which initiates at the FMCS, consistently occurs in the regions that are aligned along the compression direction. The initiation zones are localised in specific areas depending

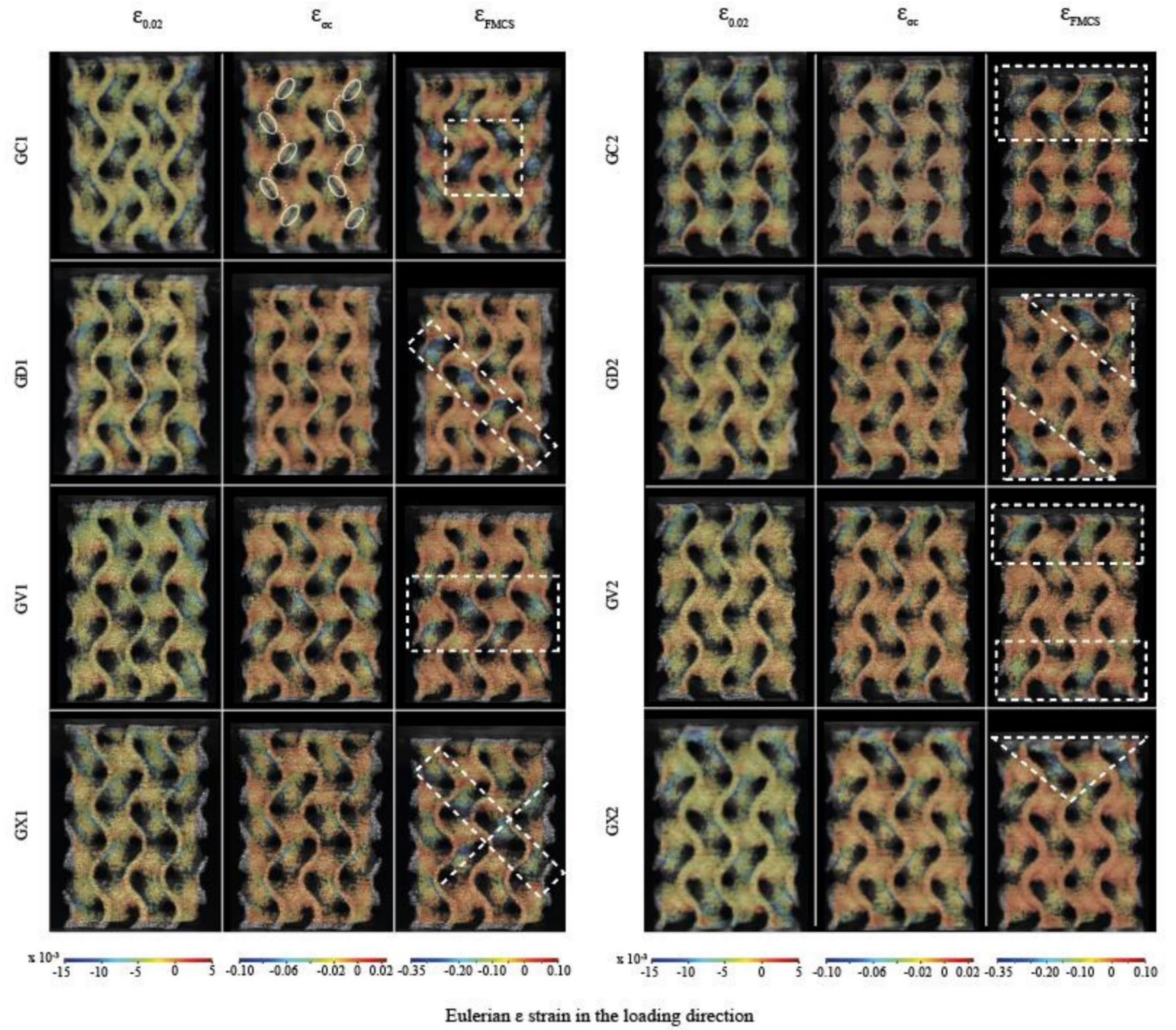

**Fig. 11** Eulerian longitudinal strain obtained from DIC analysis. In blue compressive strains, while in red traction strains. The snake-like geometry highlighted in GC1 $\varepsilon_{\sigma c}$ represents the localised steep gradients that occur across the channel regions where the failure starts. The dashed boxes at the FMCS highlight the localised strain concentration zones, which correlate with the subsequent failure sites

on the gradation patterns and are highlighted in the dashed regions in Fig. 11. These varying thicknesses within the geometry, based on the type of initiator surfaces, perturb the propagation mechanism along the diagonal shear bands through density variations. As a result, the failure modes that arise are contingent upon the gradation pattern that is implemented. Overall, for the mechanical performances, higher values are obtained at incremental values of average relative density, with average relative densities ranging from approximately 20% (GUT1) to 35% (GUT2) as discussed in the morphological characterisation section (Sect. 3.1). The C and X type gradations were respectively the most rigid and least rigid in the G1 group, and vice versa for the G2 type group.

The behaviour of the different structures is discussed here for each geometry in detail:

- Core (GC). The mechanical response of core structures (GC) is comparable to that of the uniform thickness, with GC2 comparable to GUT1 and GC1 comparable to GUT2. However, from the DIC analysis (Fig. 11), the GC2 specimen displayed overall lower compressive strains than GUT1, starting from global strains corresponding to $\varepsilon_{\sigma c}$. Specifically, GC2 shows better distributed local strains, with fewer tensile strain concentra-

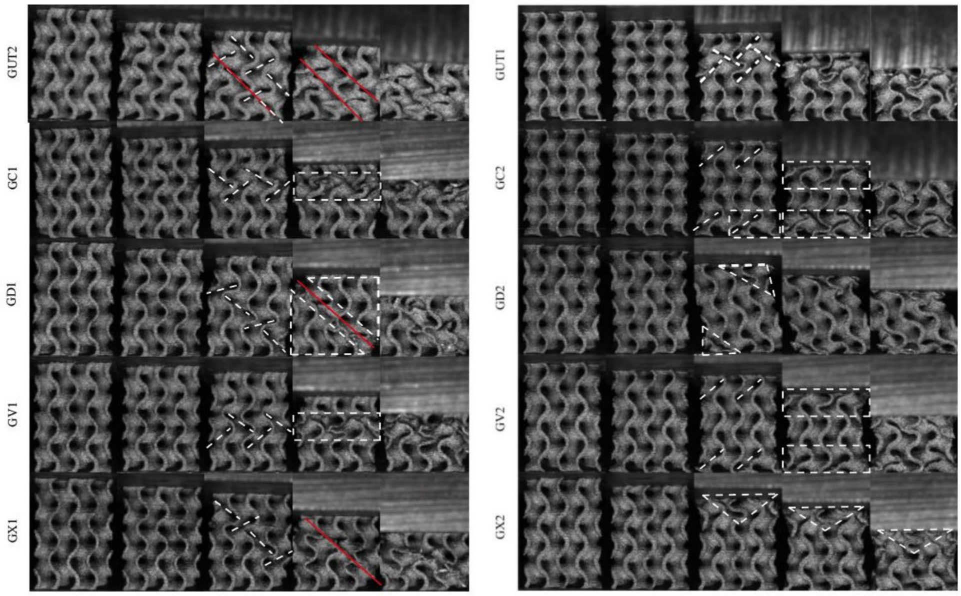

**Fig. 12** Deformation behaviour and failure modes. The dashed lines represent the localised initial failure sites occurring in the regions near the channels. The dashed box represents instead the regions subjected to global failure, while the red lines highlight the observed diagonal shear bands

tions in the regions near the channels (Fig. 11). This improved strain distribution resulted in a 17% increase in stiffness (i.e. quasi elastic gradient) compared to the uniform GUT1 structure despite having an almost identical FMCS. At the onset of the instability peak, the thicker core characteristic of GC2 structure provides structural rigidity in the central region of the specimen, confining the higher strains to the upper and lower regions characterised by a lower density (dashed box in Fig. 11). This behaviour results in instability loads similar to GUT1 because the failure occurs in the areas with a reduced thickness. The structure collapse begins with the failure of the lower right foot, as shown in Fig. 12, where the concentration of tensile strains reaches the material limit at the surface with higher curvature of the corresponding channel. The structure then fails in the lower region, with a redistribution of the load to the other cells and subsequently failing in the upper region with the same dynamics, leading to the onset of a second load peak. The failure continues with the compaction of the specimen along the loading direction, regaining load-bearing capacity due to the compression of the higher-density core. This is also visible in the stress–strain curve (Fig. 9), with a peak at higher values due to the higher density of the region. The failure is progressive, with the upper and lower regions failing sequentially, followed by the crushing of the reinforcing core, leading to a stable plateau at 46.9 MPa. On the other hand, the strain field of specimen GC1 reveals that at a global strain corresponding to $\varepsilon_{\sigma c}$, the highest deformations are concentrated along the outer snake-like geometries located at the sides of the specimen, as highlighted in Fig. 11. This contrasts with specimen GUT1, where the strain is primarily localised around the central snake-like structure (Fig. 10). This difference is particularly noticeable in the strain fields at global strains corresponding to $\varepsilon_{0.02}$ and $\varepsilon_{\sigma c}$. This phenomenon is likely due to the concentrations of the strains occurring in the less dense core caused by the applied gradation pattern, which, upon yielding, redistributes the load-bearing capacity to the sides of the specimen, which are thicker. Approaching the FMCS, GC1 shows a concentration of high local compressive strain areas in the central region of the specimen (dashed box Fig. 11), differently from GUT2 characterised by a uniform strain distribution. This behaviour is probably due to the thinner core of the structure, which loses bearing capacity. The structure fails in the central section (Fig. 12) at a global strain 5% lower than the strain corresponding to the FMCS of GUT2. Compared to the uniform density specimen, GC1 shows a smaller peak drop, and from strain higher than 20%, it behaves like GUT2, exhibiting a steepening of the sigma-epsilon response typical for thicker gyroid structures [8, 65]. Ultimately, differently from the findings reported by Ref. [38], the Core (GC) structure did not demonstrate substantial improvement in mechanical performances, but it exhibited distinct failure mechanisms compared to the uniform specimens, without developing typical diagonal shear bands. However, a comparison with the uniform reference structures is missing in Ref. [38].

- Diagonal (GD). The GD1 and GD2 structures show almost overlapping mechanical responses that slightly differ from GUT1, as shown in Fig. 9, with quasi elastic-gradient of 2050 MPa and 1810 MPa, respectively and equal values of FMCS (75 MPa). The analysis of the strain field for the GD1 shows that at the global strain corresponding to $\varepsilon_{\sigma c}$, a strain concentration occurs on the less dense diagonal where the gradation pattern is applied. The other thicker regions of the specimen displayed more homogeneous and lower strain values. The concentration deformations in the region of the thinner diagonal overlap with the typical failure mode of the gyroid structure, where collapse originates due to the development of diagonal shear bands (red line in Fig. 12). The thinner diagonal thus promotes this type of structural failure, resulting in a predictable and preferential failure site highlighted in Fig. 11. The specimen separates into two halves (Fig. 12) that compress and compact against each other, recovering structural capacity and causing the steepening of the stress–strain response as shown in Fig. 9. GD2, instead, had an unstable behaviour under the compression load, tilting counterclockwise (Fig. 12). This rotation is caused by the subsequent failure of the triangular region with lower density highlighted in Fig. 12. This rotation may originate from the low number of cells with high thickness (along the initiator surface) present in the considered structures. A larger number of cells along the initiator surface may mitigate the rotation of the structure and compensate for it. The effect of the strain distribution and the rotation of the sample is also visible in the strain field represented in Fig. 11. The thinner areas of the samples experience a strain concentration, while the thicker diagonal remains almost unloaded. From the stress–strain curve for the sample GD2 reported in Fig. 9, it can be seen that after an initial instability peak caused by the failure of the thinner triangular regions of the sample, there is a recovery of load-bearing capacity due to the reorientation of the diagonal region, resulting in a higher slope of the plateau region, similar to the behaviour of GUT2. The strain concentration at the corners is already clearly visible at a global strain of $\varepsilon_{0.02}$ (Fig. 11). Indeed, the denser region shows uniformly lower strains (extended orange region).

- Vertical (GV). Considering the stress–strain curve, the structures with a vertical gradation, GV1 and GV2, as the diagonal structures, displayed similar mechanical responses, with 30% more stiffness in GV2 and an overlap of FMCS at 84 MPa. As a consequence of the strain concentration in the lower density regions, in agreement with the findings of Onal et al. [66], GV1 exhibited a predictable failure mode starting in the central layer (dashed box in Fig. 11). After the initial collapse, the structure compacts, regaining load-bearing capacity. Following the FMCS and the failure of the central structure, two more peaks are observed, corresponding to the failure and subsequent structural recovery of the other two rows of thicker cells. For GV2, instead, similar to GD2, the larger deformations concentrate in the lower-density regions at the top and bottom of the specimen (dashed boxes in Fig. 11), while uniformly distributing the compressive strains in the central, thicker region. Upon reaching the FMCS, failure begins in the lower region and occurs in the upper region (dashed lines in Fig. 12). The progressive failure of the lower region first and the upper region after results in a plateau region with a strain similar to that of the FMCS, which remains constant up to a global strain of 25%. The plateau region is followed by a recovery of load-bearing capacity due to the specimen compacting in the central region with double thickness.
- Cross (GX). The cross-pattern gradation, differently from the D and V, presents marked differences in terms of mechanical performances between GX1 and GX2. GX2 is 35% stiffer with an FMCS of almost 120 MPa, approximately 50% higher than GX1. In GX1, the larger deformations concentrate on the thinner diagonals, as visible in the strain fields shown in Fig. 11. In proximity to the FMCS occurrence, one of the two diagonals fails in a brittle manner (red line in Fig. 12), causing the specimen to split into two halves that progressively slide along the fracture plane under load, gradually regaining load-bearing capacity. The FMCS occurs at slightly higher global strains than GD1, likely due to the strain perturbation caused by the second diagonal perpendicular to the one where structural failure occurred. Unlike the other structures with an initiator surface of 0.7 mm, a more stable plateau is observed after the initial instability peak, ensuring constant loads due to the progressive crushing of the structure. In GX2, instead, the thicker diagonals confine the higher deformations in the upper and lower triangular regions with lower density, leading to the onset of FMCS. After the failure of the upper region, the instability progressively propagates along the height of the specimen with progressive layer-by-layer crushing. This characteristic gives the corresponding mechanical response an extremely extended plateau region at constant load up to global strain values of 50%.

In light of the observed mechanical behaviour, the structures also differ remarkably in terms of absorbed energy. Figure 13 shows the energy absorption characteristics of the structures considered in this work. Figure 13a and b show the absorbed energy, while Fig. 13c and d show the energy absorption efficiency. For the energy absorption capabilities, the reference uniform structures GUT1 and GUT2 displayed values of 21.9 J/mm$^3$ and 68 J/mm$^3$ at a global strain of 50%, respectively. GC2 displayed the lowest performance in terms of cumulative absorbed energy per unit volume (23.5 J/mm$^3$) among the thickness-graduated structures, slightly higher than GUT1 (21.9 J/mm$^3$). As shown in Table 2 and Fig. 13c and d, considering the energy absorption capacity, the specimens can be divided into two distinct groups. GC2, GX1,

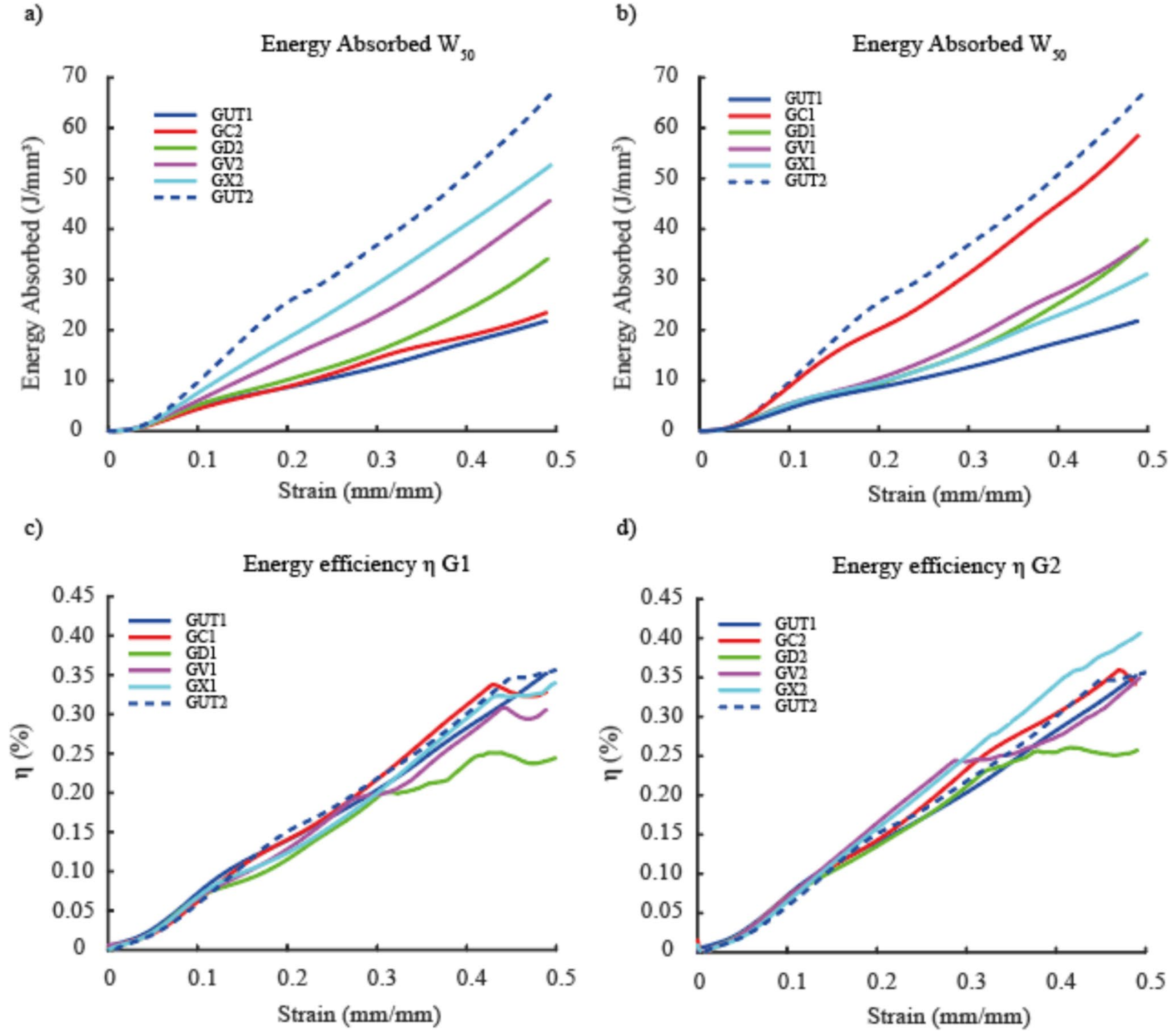

**Fig. 13** Cumulative energy absorption per unit volume and efficiency plots

GD2, GV1 and GD1 fell within a range of 23 J/mm$^3$ to 38 J/mm$^3$. The last group is formed by GV2, GX2, and GC1, with maximum values between 45.8 J/mm$^3$ and 58.6 J/mm$^3$. In terms of SEA, GUT1 and GUT2 are characterised by a value of 2.8E7 J/kg and 4.5E7 J/kg. The distinction between the two groups is also valid when considering the SEA. The first group, including GC2, GD2, GD1, GV1 and GX1, is characterised by values of SEA ranging from 2.7E7 J/kg to 3.3 J/kg. The second group includes the structures GV2, GX2 and GC1 with values of SEA ranging from 4.0E7 J/kg to 4.2E7 J/kg. Higher values of $W_{50}$ and SEA are achievable in the cases where failure occurs progressively in multiple stages with subsequent drops after the FMCS of reduced magnitude, as occurred for GV2, GX2, and GC1. Regarding the absorbed energy, a better performance is obtained for gradations that allow for initial preferential failure at the specimen extremities relative to the compression axis (i.e., in the upper and lower regions of GV2, GX2, and GC1 specimens highlighted in Fig. 12). Progressive failure of the extremities allows the specimens to concentrate on the denser and thus more rigid core, ensuring better absorption capacity compared to failures localised in the central region of the specimens, complete detachment failure planes, or rotations under load. The poorest performance in terms of energy absorption and Specific Energy Absorption (SEA) is displayed by GC2, which shows a SEA value even lower than that of the uniform GUT1. This behaviour is likely attributable to the core gradation design, where a thicker graded sphere at the structure's centre shifts deformation towards the thinner extremities, thereby reducing the overall energy absorption capacity. In terms of energy absorption efficiency (Fig. 13c and d) all gradations, except for the diagonal pattern, exhibit similar trends. The structures in group G1 exhibited higher efficiencies calculated at a 50% global strain, ranging between 35 and 41%, while the structures in group G2 displayed values approximately 5% lower than those of the first group. In both cases, the D-type geometry exhibited the worst performances in terms of efficiency, reaching an efficiency of approximately 25% at a global strain value close to 35%. The peaks observable in the energy absorption efficiency represents the moments of densification, where the peak stress exhibited by the structures exceeds the FMCS value. At these global strain values, there is significant compaction of the structure, leading to the re-establishment of contact between the failed and heavily deformed zones and the remaining structures, resulting in an increase in the load-bearing capacity.

To contextualise the results obtained for the 3D graded structures, the review paper by Noronha et al. [37] is used as a benchmark for one-dimensional graded lattices. The comparison indicates that the 3D graded structures are well-positioned in terms of Young's modulus. Within the same relative density range considered in this study, the review by Noronha et al. [37] includes only a limited set of one-dimensional graded topologies. In comparison, the 3D graded structures investigated here demonstrate improved stiffness and enhanced energy absorption capabilities, despite being composed of fewer unit cells. For the same topology, in comparison with one-dimensional grading structures at lower relative density, the 3D graded structures appeared weaker. However, it should be noted that the data reported in Ref. [37] refer to gyroid samples with a higher number of cells (see, for example, [70]). Despite considering a lower number of cells in our analysis, the performed 3D graded patterns still demonstrated an excellent capability for tuning mechanical performance. Regarding energy absorption, and independently of the relative density, the 3D graded structures generally demonstrate superior performance. This remains true even considering that the energy absorption values in Ref. [37] were calculated either at complete densification of the structure or at the end strain plateau, highlighting the inconsistency present in ISO 13314:2011. The standard indeed suggests the possibility of using different notable points in the stress–strain response for calculating the absorbed energy, such as at a total strain of 50%, as in the current study.

## 4 Conclusion

This paper introduces novel lattice structures based on TPMS design, which considers a three-dimensional gradation of thickness along different directions with respect to the build direction. 30 samples were produced using the PBF-EB technique and characterised in terms of morphology, mechanical characteristics and deformation behaviour. The effect of the manufacturing process produced discrepancies between the manufactured and designed structure, which were more pronounced in structures with higher relative densities. These effects are due to thermal effects and volume shrinkage.

The mechanical characterisation of the graded structures revealed significant insights into their deformation behaviour captured by 2D-DIC analysis and energy absorption capabilities. The stress–strain curves indicated that the mechanical responses of the graded structures lie between those of the uniform thickness reference structures, with variations in strain distribution and failure modes due to the applied gradation patterns. The 3D gradation overall produced a significant enhancement in mechanical performance, particularly in terms of energy absorption capabilities, stiffness, and FMCS when compared to the structure with uniform minimum thickness. This comes practically at no weight cost because the relative density is only slightly increased. As an example, comparing the structure GX1 to GUT1, with a modest increase of density of approximately 8%, GX1 shows an increase of 88% for the FMCS, 22% for the plateau stress and 9% for the SEA. The observed localised strain concentrations in the lower relative density regions facilitate the production of highly specific energy-absorptive structures, which are capable of resisting further damage, as a result of the improved load-bearing capacity and strength recovery. This behaviour resulted in significant improvements in energy absorption capabilities, making it beneficial for applications requiring sustained load-bearing capacity under progressive deformation. Indeed, when evaluating the specific energy absorption (SEA) relative to the volume of material used, GV2 and GX2 demonstrated superior energy absorption efficiency. At slightly higher relative densities, approximately between 25 and 28%, roughly the midpoint of the range considered in this study, the progressive failure of the lower and upper regions promoted the development of a stable and extended plateau region, effectively maintaining load-bearing capacity despite initial structural instabilities.

Besides the improved efficiency in terms of energy absorption and mechanical properties, grading of the wall thickness provides a tool for tuning the mechanical behaviour of the structure. As an example, according to the wall thickness gradation, it is possible to control the width of the $\sigma_{pl}$, control the quasi elastic gradient, control the deformation behaviour of the structure under compression load or the failure site. Uniform thickness structures somehow constrain the designer's freedom, forcing them to accept a compromise. The graded structures provided an additional degree of autonomy, enabling designers to create the most suitable structure for each specific application without introducing a substantial increase in material use.

As a conclusive remark, the authors wish to emphasise that, while relative density remains a useful starting point for interpreting the mechanical performance of lattice structures, it appears insufficient for accurately describing or predicting the behaviour of real, complex, additively manufactured lattices. The relative density provides a scalar value which fails to capture critical geometric features such as unit cell topology, the number of unit cells involved, and the distribution of wall thickness. As demonstrated in this study, also through DIC analysis, load paths are highly dependent on the architecture and connectivity of the structure, and both stress distribution and failure localisation are strongly influenced by these geometric characteristics. As lattice designs move further away from simple, ordered, periodically repeated unit cells in three-dimensional space, it becomes increasingly important to establish new descriptors and guidelines to support a more informed, application-driven design approach.

**Acknowledgements** Simone De Giorgi is kindly acknowledged for executing the tomographies.

**Author Contribution** Conceptualization M.G and G.R; Methodology G.R, M.G and D.B; Data curation, Formal analysis, Investigation, Visualization and Writing – original draft D.B and G.R; Supervision and Writing – review & editing M.G.

**Funding** Open access funding provided by Politecnico di Torino within the CRUI-CARE Agreement. European Union—NextGenerationEU Sustainable Mobility Center, CN00000023.

**Data Availability** No datasets were generated or analysed during the current study.

## Declarations

**Competing Interests** The authors declare no competing interests.

## References

1. Hooke R (1665) Micrographia, or, some physiological descriptions of minute bodies made by magnifying glasses with observations and inquiries thereupon. Jo. Martyn and Ja. Allestry, printers to the Royal Society, London
2. Singh S, Bhatnagar N (2018) A survey of fabrication and application of metallic foams (1925–2017). J Porous Mater 25:537–554. https://doi.org/10.1007/s10934-017-0467-1
3. Maiti SK, Gibson LJ, Ashby MF (1984) Deformation and energy absorption diagrams for cellular solids. Acta Metall 32:1963–1975. https://doi.org/10.1016/0001-6160(84)90177-9
4. Gibson LJ, Ashby MF, Harley BA (2010) Cellular materials in nature and medicine. Cambridge University Press
5. Gibson LJ, Ashby MF (1982) The mechanics of three-dimensional cellular materials. Proc R Soc Lond Math Phys Sci 382:43–59. https://doi.org/10.1098/rspa.1982.0088
6. Helou M, Kara S (2018) Design, analysis and manufacturing of lattice structures: an overview. Int J Comput Integr Manuf 31:243–261. https://doi.org/10.1080/0951192X.2017.1407456
7. Tan XP, Tan YJ, Chow CSL et al (2017) Metallic powder-bed based 3D printing of cellular scaffolds for orthopaedic implants: a state-of-the-art review on manufacturing, topological design, mechanical properties and biocompatibility. Mater Sci Eng, C 76:1328–1343. https://doi.org/10.1016/j.msec.2017.02.094
8. du Plessis A, Razavi N, Benedetti M et al (2022) Properties and applications of additively manufactured metallic cellular materials: a review. Prog Mater Sci 125:100918. https://doi.org/10.1016/j.pmatsci.2021.100918
9. Bhate D (2019) Four questions in cellular material design. Materials 12:1060. https://doi.org/10.3390/ma12071060
10. Pan C, Han Y, Lu J (2020) Design and optimization of lattice structures: a review. Appl Sci 10:6374. https://doi.org/10.3390/app10186374
11. Hyde S, Blum Z, Landh T et al (1996) The language of shape: the role of curvature in condensed matter: Physics, Chemistry and Biology. Elsevier
12. Jinnai H, Nishikawa Y, Ito M et al (2002) Topological similarity of sponge-like bicontinuous morphologies differing in length scale. Adv Mater 14:1615–1618. https://doi.org/10.1002/1521-4095(20021118)14:22%3c1615::AID-ADMA1615%3e3.0.CO;2-S
13. Jinnai H, Watashiba H, Kajihara T et al (2002) Surface curvatures of trabecular bone microarchitecture. Bone 30:191–194. https://doi.org/10.1016/S8756-3282(01)00672-X
14. Zadpoor AA (2015) Bone tissue regeneration: the role of scaffold geometry. Biomater Sci 3:231–245. https://doi.org/10.1039/C4BM00291A
15. Fashanu O, Rangapuram M, Abutunis A et al (2022) Mechanical performance of sandwich composites with additively manufactured triply periodic minimal surface cellular structured core. J Sandw Struct Mater 24:1133–1151. https://doi.org/10.1177/10996362211037012
16. Speirs M, Van Hooreweder B, Van Humbeeck J, Kruth J-P (2017) Fatigue behaviour of *NiTi* shape memory alloy scaffolds produced by SLM, a unit cell design comparison. J Mech Behav Biomed Mater 70:53–59. https://doi.org/10.1016/j.jmbbm.2017.01.016

17. Feng J, Fu J, Yao X, He Y (2022) Triply periodic minimal surface (TPMS) porous structures: from multi-scale design, precise additive manufacturing to multidisciplinary applications. Int J Extreme Manuf 4:22001. https://doi.org/10.1088/2631-7990/ac5be6
18. Khrapov D, Kozadayeva M, Manabaev K et al (2021) Different approaches for manufacturing Ti-6Al-4V alloy with triply periodic minimal surface sheet-based structures by electron beam melting. Materials 14:4912. https://doi.org/10.3390/ma14174912
19. Rizza G, Galati M, Iuliano L (2022) A phase-field study of neck growth in electron beam powder bed fusion (EB-PBF) process of Ti6Al4V powders under different processing conditions. Int J Adv Manuf Technol 123:855–873. https://doi.org/10.1007/s00170-022-10204-4
20. Rizza G, Galati M (2024) Powder bed fusion with electron beam: the interplay of sintering, porosity, and coordination number in modelling the powder thermal conductivity through a novel tortuosity formulation. Int J Heat Mass Transf 234:126055. https://doi.org/10.1016/j.ijheatmasstransfer.2024.126055
21. Khrapov D, Kozadayeva M, Koptyug A et al (2023) Geometrical features and mechanical properties of the sheet-based gyroid scaffolds with functionally graded porosity manufactured by electron beam melting. Mater Today Commun 35:106410. https://doi.org/10.1016/j.mtcomm.2023.106410
22. Sokollu B, Gulcan O, Konukseven EI (2022) Mechanical properties comparison of strut-based and triply periodic minimal surface lattice structures produced by electron beam melting. Addit Manuf 60:103199. https://doi.org/10.1016/j.addma.2022.103199
23. Khrapov D, Paveleva A, Kozadayeva M et al (2023) Trapped powder removal from sheet-based porous structures based on triply periodic minimal surfaces fabricated by electron beam powder bed fusion. Mater Sci Eng A 862:144479. https://doi.org/10.1016/j.msea.2022.144479
24. Khrapov D, Koptyug A, Surmenev R, Surmeneva M (2024) Expanding manufacturability of sheet-based triply periodic minimal surfaces by electron beam powder bed fusion in wafer theme. Mater Today Commun 40:109580. https://doi.org/10.1016/j.mtcomm.2024.109580
25. Zhao S, Li SJ, Wang SG et al (2018) Compressive and fatigue behavior of functionally graded Ti-6Al-4V meshes fabricated by electron beam melting. Acta Mater 150:1–15. https://doi.org/10.1016/j.actamat.2018.02.060
26. Ataee A, Li Y, Fraser D et al (2018) Anisotropic Ti-6Al-4V gyroid scaffolds manufactured by electron beam melting (EBM) for bone implant applications. Mater Des 137:345–354. https://doi.org/10.1016/j.matdes.2017.10.040
27. Polley C, Radlof W, Hauschulz F et al (2022) Morphological and mechanical characterisation of three-dimensional gyroid structures fabricated by electron beam melting for the use as a porous biomaterial. J Mech Behav Biomed Mater 125:104882. https://doi.org/10.1016/j.jmbbm.2021.104882
28. Peng X, Huang Q, Zhang G et al (2022) Compensating the anisotropic mechanical properties of electron beam melting-based gyroid scaffolds using structural design. Int J Mech Sci 226:107442. https://doi.org/10.1016/j.ijmecsci.2022.107442
29. Lin Z, Dadbakhsh S, Rashid A (2022) Developing processing windows for powder pre-heating in electron beam melting. J Manuf Process 83:180–191. https://doi.org/10.1016/j.jmapro.2022.08.063
30. Drescher P, Reimann T, Seitz H (2014) Investigation of powder removal of net-structured titanium parts made from electron beam melting. Int J Rapid Manuf 4:81. https://doi.org/10.1504/IJRAPIDM.2014.066007
31. Yao B, Zhang Z, Li Z et al (2024) Compressive properties and energy absorption of selective laser melting formed Ti-6Al-4V porous radial gradient scaffold. Powder Technol 442:119856. https://doi.org/10.1016/j.powtec.2024.119856
32. Araya M, Jaskari M, Rautio T et al (2024) Assessing the compressive and tensile properties of TPMS-gyroid and stochastic Ti64 lattice structures: a study on laser powder bed fusion manufacturing for biomedical implants. J Sci: Adv Mater Devices 9:100663. https://doi.org/10.1016/j.jsamd.2023.100663
33. Tilton M, Borjali A, Isaacson A et al (2021) On structure and mechanics of biomimetic meta-biomaterials fabricated via metal additive manufacturing. Mater Des 201:109498. https://doi.org/10.1016/j.matdes.2021.109498
34. (2012) ISO 13314:2011 mechanical testing of metals — ductility testing — compression test for porous and cellular metals
35. Liu F, Mao Z, Zhang P et al (2018) Functionally graded porous scaffolds in multiple patterns: new design method, physical and mechanical properties. Mater Des 160:849–860. https://doi.org/10.1016/j.matdes.2018.09.053
36. Zhang X-Y, Yan X-C, Fang G, Liu M (2020) Biomechanical influence of structural variation strategies on functionally graded scaffolds constructed with triply periodic minimal surface. Addit Manuf 32:101015. https://doi.org/10.1016/j.addma.2019.101015
37. Noronha J, Dash J, Leary M et al (2023) Additively manufactured functionally graded lattices: design, mechanical response, deformation behavior, applications, and insights. JOM 75:5729–5754. https://doi.org/10.1007/s11837-023-06190-x
38. Gandhi R, Salmi M, Roy B et al (2025) Mechanical and fatigue performance of multidirectional functionally graded Ti6Al4V scaffolds produced via laser powder bed fusion for orthopedic implants. Mater Des 251:113725. https://doi.org/10.1016/j.matdes.2025.113725
39. Hao B, Zhu Z, Zhang L (2024) Network-based and sheet-based gyroid lattice structures with different gradient directions: manufacture, mechanical response and energy absorption. Meccanica 59:1911–1926. https://doi.org/10.1007/s11012-024-01874-3
40. Rahmat N, Kadkhodapour J, Arbabtafti M (2023) Mechanical characterization of additively manufactured orthopedic cellular implants: case study on different cell types and effect of defects. Phys Mesomech 26:443–458. https://doi.org/10.1134/S1029959923040069
41. Karuna C, Poltue T, Khrueaduangkham S, Promoppatum P (2022) Mechanical and fluid characteristics of triply periodic minimal surface bone scaffolds under various functionally graded strategies. J Comput Des Eng 9:1258–1278. https://doi.org/10.1093/jcde/qwac052
42. Caiazzo F, Alfieri V, Guillen DG, Fabbricatore A (2022) Metal functionally graded gyroids: additive manufacturing, mechanical properties, and simulation. Int J Adv Manuf Technol 123:2501–2518. https://doi.org/10.1007/s00170-022-10334-9
43. Fan Z, Huang G, Lu Y et al (2022) Full compression response of FG-based scaffolds with varying porosity via an effective numerical scheme. Int J Mech Sci 223:107294. https://doi.org/10.1016/j.ijmecsci.2022.107294
44. Schoen AH (1970) Infinite periodic minimal surfaces without self-intersections. National Aeronautics and Space Administration
45. Michielsen K, Kole JS (2003) Photonic band gaps in materials with triply periodic surfaces and related tubular structures. Phys Rev B 68:115107. https://doi.org/10.1103/PhysRevB.68.115107
46. Wohlgemuth M, Yufa N, Hoffman J, Thomas EL (2001) Triply periodic bicontinuous cubic microdomain morphologies by symmetries. Macromolecules 34:6083–6089. https://doi.org/10.1021/ma0019499
47. von Schnering HG, Nesper R (1991) Nodal surfaces of fourier series: fundamental invariants of structured matter. Z Phys B Condens Matter 83:407–412. https://doi.org/10.1007/BF01313411
48. Klinowski J, Mackay AL, Humberto T (1996) Curved surfaces in chemical structure. Philos Trans R Soc Lond Ser Math Phys Eng Sci 354:1975–1987. https://doi.org/10.1098/rsta.1996.0086

49. Al-Ketan O, Abu Al-Rub RK (2019) Multifunctional mechanical metamaterials based on triply periodic minimal surface lattices. Adv Eng Mater 21:1900524. https://doi.org/10.1002/adem.201900524
50. Galati M, Giordano M, Iuliano L (2023) Process-aware optimisation of lattice structure by electron beam powder bed fusion. Prog Addit Manuf 8:477–493. https://doi.org/10.1007/s40964-022-00339-x
51. Al-Saedi DSJ, Masood SH, Faizan-Ur-Rab M et al (2018) Mechanical properties and energy absorption capability of functionally graded F2BCC lattice fabricated by SLM. Mater Des 144:32–44. https://doi.org/10.1016/j.matdes.2018.01.059
52. Yang L, Mertens R, Ferrucci M et al (2019) Continuous graded gyroid cellular structures fabricated by selective laser melting: design, manufacturing and mechanical properties. Mater Des 162:394–404. https://doi.org/10.1016/j.matdes.2018.12.007
53. Boivineau M, Cagran C, Doytier D et al (2006) Thermophysical properties of solid and liquid Ti-6Al-4V (TA6V) alloy. Int J Thermophys 27:507–529. https://doi.org/10.1007/PL00021868
54. Vanderesse N, Richter A, Nuño N, Bocher P (2018) Measurement of deformation heterogeneities in additive manufactured lattice materials by digital image correlation: strain maps analysis and reliability assessment. J Mech Behav Biomed Mater 86:397–408. https://doi.org/10.1016/j.jmbbm.2018.07.010
55. Chen W-M, Xie YM, Imbalzano G et al (2016) Lattice Ti structures with low rigidity but compatible mechanical strength: design of implant materials for trabecular bone. Int J Precis Eng Manuf 17:793–799. https://doi.org/10.1007/s12541-016-0097-6
56. Blaber J, Adair B, Antoniou A (2015) Ncorr: open-source 2D digital image correlation matlab software. Exp Mech 55:1105–1122. https://doi.org/10.1007/s11340-015-0009-1
57. Jones E, Iadicola M, Bigger R, et al (2018) A good practices guide for digital image correlation. International Digital Image Correlation Society
58. Lecompte D, Smits A, Bossuyt S et al (2006) Quality assessment of speckle patterns for digital image correlation. Opt Lasers Eng 44:1132–1145. https://doi.org/10.1016/j.optlaseng.2005.10.004
59. Kotzem D, Höffgen A, Raveendran R et al (2022) Position-dependent mechanical characterization of the PBF-EB-manufactured Ti6Al4V alloy. Prog Addit Manuf 7:249–260. https://doi.org/10.1007/s40964-021-00228-9
60. Galati M, Rizza G, Defanti S, Denti L (2021) Surface roughness prediction model for electron beam melting (EBM) processing Ti6Al4V. Precis Eng 69:19–28. https://doi.org/10.1016/j.precisioneng.2021.01.002
61. Al-Bermani SS, Blackmore ML, Zhang W, Todd I (2010) The origin of microstructural diversity, texture, and mechanical properties in electron beam melted Ti-6Al-4V. Metall Mater Trans A 41:3422–3434. https://doi.org/10.1007/s11661-010-0397-x
62. Jamshidinia M, Kovacevic R (2015) The influence of heat accumulation on the surface roughness in powder-bed additive manufacturing. Surf Topogr Metrol Prop 3:14003. https://doi.org/10.1088/2051-672X/3/1/014003
63. Smith CJ, Derguti F, Hernandez Nava E et al (2016) Dimensional accuracy of electron beam melting (EBM) additive manufacture with regard to weight optimized truss structures. J Mater Process Technol 229:128–138. https://doi.org/10.1016/j.jmatprotec.2015.08.028
64. Wang C, Sun C-N, Zhang L et al (2024) Improving component dimensional accuracy in electron beam powder bed fusion by addressing nonlinear deformations with 3D compensation strategies. Virtual Phys Prototyping 19:e2430319. https://doi.org/10.1080/17452759.2024.2430319
65. Fan X, Tang Q, Feng Q et al (2021) Design, mechanical properties and energy absorption capability of graded-thickness triply periodic minimal surface structures fabricated by selective laser melting. Int J Mech Sci 204:106586. https://doi.org/10.1016/j.ijmecsci.2021.106586
66. Onal E, Frith JE, Jurg M et al (2018) Mechanical properties and in vitro behavior of additively manufactured and functionally graded Ti6Al4V porous scaffolds. Metals 8:200. https://doi.org/10.3390/met8040200
67. Downing D, Jones A, Brandt M, Leary M (2021) Increased efficiency gyroid structures by tailored material distribution. Mater Des 197:109096. https://doi.org/10.1016/j.matdes.2020.109096
68. Shi W, Lin Y, Li J et al (2024) Optimization of mechanical properties of Ti–6Al–4V triply periodic minimal surface porous structures prepared by laser beam powder bed fusion technology based on orientation control. Mater Sci Eng A 894:146183. https://doi.org/10.1016/j.msea.2024.146183
69. Maskery I, Aboulkhair NT, Aremu AO et al (2017) Compressive failure modes and energy absorption in additively manufactured double gyroid lattices. Addit Manuf 16:24–29. https://doi.org/10.1016/j.addma.2017.04.003
70. Al-Ketan O, Lee D-W, Rowshan R, Abu Al-Rub RK (2020) Functionally graded and multi-morphology sheet TPMS lattices: design, manufacturing, and mechanical properties. J Mech Behav Biomed Mater 102:103520. https://doi.org/10.1016/j.jmbbm.2019.103520